



January 2012

# Assessment Of Nasa Giss C mip5 Modele Simulated Clouds And Toa Radiation Budgets Using Satellite Observations Over The Southern Mid-Latitudes

Ryan Evan Stanfield

Follow this and additional works at: <https://commons.und.edu/theses>

---

## Recommended Citation

Stanfield, Ryan Evan, "Assessment Of Nasa Giss C mip5 Modele Simulated Clouds And Toa Radiation Budgets Using Satellite Observations Over The Southern Mid-Latitudes" (2012). *Theses and Dissertations*. 1380.  
<https://commons.und.edu/theses/1380>

This Thesis is brought to you for free and open access by the Theses, Dissertations, and Senior Projects at UND Scholarly Commons. It has been accepted for inclusion in Theses and Dissertations by an authorized administrator of UND Scholarly Commons. For more information, please contact [zeinebyousif@library.und.edu](mailto:zeinebyousif@library.und.edu).

ASSESSMENT OF NASA GISS CMIP5 MODELE SIMULATED CLOUDS AND  
TOA RADIATION BUDGETS USING SATELLITE OBSERVATIONS  
OVER THE SOUTHERN MID-LATITUDES

by

Ryan Evan Stanfield  
Bachelor of Science, Texas A&M University, 2008

A Thesis  
Submitted to the Graduate Faculty

of the

University of North Dakota

in partial fulfillment of the requirements

for the degree of

Master of Science

Grand Forks, North Dakota  
December  
2012

Copyright 2012 Ryan Stanfield

This thesis, submitted by Ryan Stanfield in partial fulfillment of the requirements for the Degree of Master of Science from the University of North Dakota, has been read by the Faculty Advisory Committee under whom the work has been done, and is hereby approved.



---

Xiquan Dong



---

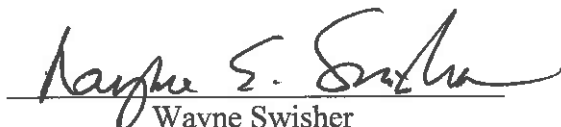
Baike Xi



---

Michael Poellot

This thesis is being submitted by the appointed advisory committee as having met all of the requirements of the Graduate School at the University of North Dakota and is hereby approved.



---

Wayne Swisher  
Dean of the Graduate School



---

Date

PERMISSION

Title            Assessment of NASA GISS CMIP5 ModelE Simulated Clouds and TOA  
Radiation Budgets Using Satellite Observations over the Southern Mid-  
Latitudes

Department    Atmospheric Sciences

Degree         Master of Science

In presenting this thesis in partial fulfillment of the requirements for a graduate degree from the University of North Dakota, I agree that the library of this University shall make it freely available for inspection. I further agree that permission for extensive copying for scholarly purposes may be granted by the professor who supervised my thesis work or, in his absence, by the Chairperson of the department or the dean of the Graduate School. It is understood that any copying or publication or other use of this thesis or part thereof for financial gain shall not be allowed without my written permission. It is also understood that due recognition shall be given to me and to the University of North Dakota in any scholarly use which may be made of any material in my thesis.

Signature    Ryan Stanfield  
Date         12/06/12

## TABLE OF CONTENTS

LIST OF FIGURES .....	vii
LIST OF TABLES .....	x
ACKNOWLEDGEMENTS .....	xi
ABSTRACT.....	xiii
CHAPTER	
I.    INTRODUCTION .....	1
II.   DATA SETS .....	6
CMIP5 GISS-E2-R GCM Model Data .....	6
AMIP versus Historical Runs .....	7
Daily ISCCP Simulated Runs .....	7
Satellite Data .....	7
CERES-MODIS .....	7
CloudSat/CALIPSO (CC) .....	10
III.  METHODOLOGY .....	11
Statistical Methods .....	11
Spatial Degradation .....	12
Degradation Sensitivity .....	13
Region of Interest .....	15
IV.  RESULTS AND DISCUSSION .....	16
PART 1: Comparison of Cloud Properties .....	16

Cloud Fraction (CF) .....	16
Total Water Path (TWP).....	22
Relationship of Cloud Fraction to Optical Depth .....	25
PART 2: Impact of Clouds on the TOA Radiation Budget .....	27
Shortwave Flux .....	29
Longwave Flux .....	35
Net Flux .....	38
PART 3: Cloud Radiative Effects (CRE) .....	42
Shortwave CRE ( $CRE_{SW}$ ) .....	43
Longwave CRE ( $CRE_{LW}$ ) .....	49
Net CRE ( $CRE_{NET}$ ) .....	56
V. CONCLUSIONS .....	61
Future Work .....	69
REFERENCES .....	70

## LIST OF FIGURES

Figure	Page
1. Dark blue polygons outline regions used in SML comparisons. ....	15
2. Gridded annual mean CFs for the (a)GISS GCM, (b)SYN1 observations, and the difference (c)GISS – SYN1, for the period of March 2000 through December 2005. ....	17
3. Same as Figure 2, except split seasonally into northern hemisphere winter (DJF, left) and summer (JJA, right). ....	19
4. Vertical cloud fraction (%), as a function of cloud top pressure in millibars, for the GISS-E2-R GCM (red) over the period of March 2000 through December 2005 and for CloudSat/CALIPSO observations (CC, blue) over the period of July 2006 through June 2010. ....	21
5. Total water path (TWP) of (a)GISS, (b)SYN1, and the difference (c)GISS – SYN1, for the period of March 2000 through December 2005. ....	23
6. Same as Figure 5, except split seasonally into northern hemisphere winter (DJF, left) and summer (JJA, right). ....	25
7. Classified cloud fractions based on both optical depth and cloud-top pressure for the GISS-E2-R GCM (left) and CERES-MODIS observations (right) over the SML. ....	26
8. Same as Figure 7, except cloud classes are grouped into a 3x3 grid based on ISSCP Classifications used in Rossow and Shiffer (1999). ....	27
9. CF (top) and TWP (bottom) for the GISS GCM and CERES SYN1 results, averaged by latitude, over the period of March 2000 through December 2005. ....	28
10. Reflected shortwave radiation at TOA for the (a)GISS GCM, (b)EBAF observations, and the difference (c)GISS – EBAF, for the period of March 2000 through December 2005. ....	30
11. Same as Figure 10, except split seasonally into northern hemispheric winter (DJF, left) and summer (JJA, right). ....	31



12.	Absorbed SW radiation at TOA for the (a)GISS GCM, (b)EBAF observations, and the difference (c)GISS – EBAF, for the period of March 2000 through December 2005. ....	33
13.	Same as Figure 12, except split seasonally into northern hemispheric winter (DJF, left) and summer (JJA, right). ....	34
14.	Outgoing longwave radiation (OLR) at TOA for the (a)GISS GCM, (b)EBAF observations, and the difference (c)GISS – EBAF, for the period of March 2000 through December 2005. ....	36
15.	Same as Figure 14, except split seasonally into northern hemispheric winter (DJF, left) and summer (JJA, right). ....	37
16.	Net flux at TOA for the (a)GISS GCM, (b)EBAF observations, and the difference (c)GISS – EBAF, for the period of March 2000 through December 2005. ....	39
17.	Same as Figure 16, except split seasonally into northern hemispheric winter (DJF, left) and summer (JJA, right). ....	40
18.	Absorbed shortwave radiation, outgoing longwave radiation, and net flux for the GISS GCM and CERES EBAF results, averaged by latitude, over the period of March 2000 through December 2005. ....	41
19.	Reflected SW fluxes at TOA under clear-sky conditions for the (a)GISS GCM, (b)EBAF observations, and the difference (c)GISS – EBAF, for the period of March 2000 through December 2005. ....	44
20.	Same as Figure 19, except split seasonally into northern hemispheric winter (DJF, left) and summer (JJA, right). ....	45
21.	SW CRE at TOA for the (a)GISS GCM, (b)EBAF observations, and the difference (c)GISS – EBAF, for the period of March 2000 through December 2005. ....	47
22.	Same as Figure 21, except split seasonally into northern hemispheric winter (DJF, left) and summer (JJA, right). ....	48
23.	OLR at TOA under clear-sky conditions for the (a)GISS GCM, (b)EBAF observations, and the difference (c)GISS – EBAF, for the period of March 2000 through December 2005. ....	50
24.	Same as Figure 23, except split seasonally into northern hemispheric winter (DJF, left) and summer (JJA, right). ....	52

25.	LW CRE at TOA for the (a)GISS GCM, (b)EBAF observations, and the difference (c)GISS – EBAF, for the period of March 2000 through December 2005. ....	54
26.	Same as Figure 25, except split seasonally into northern hemisphere winter (DJF, left) and summer (JJA, right). ....	55
27.	Net CRE at TOA for the (a)GISS GCM, (b)EBAF observations, and the difference (c)GISS – EBAF, for the period of March 2000 through December 2005. ....	57
28.	Same as Figure 27, except split seasonally into northern hemispheric winter (DJF, left) and summer (JJA, right). ....	58
29.	SW, LW, and NET CRE for the GISS GCM and CERES EBAF results, averaged by latitude, over the period of March 2000 through December 2005. ....	59
30.	Taylor diagram showing the normalized global standard deviations and correlations between the GISS GCM and CERES-MODIS observations over the March 2000 to December 2005 time period. ....	65
31.	Same as Figure 30, except standard deviations and correlations are for the SML. ....	66

## LIST OF TABLES

Table	Page
1. Basic statistics used for calculating the weighted mean bias, standard deviation, and correlation between the GCM and observations. ....	11
2. Sensitivity study showing global average and standard deviation of SYN1 and EBAF data, before and after, spatial degradation through interpolation. ....	13
3. Sensitivity study showing the average and standard deviation of SYN1 and EBAF data, before and after, spatial degradation through interpolation over the southern mid-latitudes. ....	14
4. Global (GBL) weighted means, standard deviations, and correlation for the GISS GCM and CERES-MODIS Observations. ....	61
5. Weighted means, standard deviations, and correlation across the southern mid-latitudes (SML) for the GISS GCM and CERES-MODIS Observations. ....	62
6. Global (GBL) weighted means and standard deviations for the GISS GCM and CERES-MODIS Observations separated into DJF and JJA seasons. ....	63
7. Same as Table 6, except for the Southern Mid-Latitudes (SML). ....	63

## ACKNOWLEDGEMENTS

First and foremost, I would like to thank my advisor, Dr. Xiquan Dong for providing me with the opportunity to work on this research and for his guidance, expertise, and support. You for took a chance on a student with an undergraduate academic record that showed no hope of succeeding in graduate school. Thank you for giving me a chance to prove myself. Additionally, I would also like to thank the remainder of my advisement committee, Drs. Baike Xi and Michael Poellot for their comments, suggestions, and expert input into this thesis.

None of this would have been possible without my family and close friends for all their loving support and encouragement. A special thank you goes to Katie Giannecchini, for her patience, support, and for always believing in me during this process. Only you would find a way to provide such support and encouragement while over 1400 miles away. I would also like to express my appreciation for the members of my research group, as well as the remaining faculty, staff, and graduate students of the Department of Atmospheric Sciences at the University of North Dakota.

To Dr. Tony Del Genio at NASA Goddard: I would like to thank you for your questions, comments, and suggestions throughout my research. To Drs. Patrick Minnis, Dave Doelling, Norman Loeb, and Seiji Kato at the NASA Langley Research Center: I would like to thank you for your comments and suggestions in regards to my research, as well as for the data you have provided (CERES-MODIS and CloudSat/CALIPSO).

Lastly, I would like to thank all the groups involved in making all the following data available to the public. NASA GISS-E2-R data was obtained from the CMIP5 ESGF PCMDI database at <http://pcmdi9.llnl.gov/esgf-web-fe/>. CERES Terra SYN1deg-lite\_Ed2.6, CERES Aqua SYN1deg-lite\_Ed2.6, and CERES EBAF\_Ed2.6 data were obtained using the NASA Langley Research Center CERES ordering tool at <http://ceres.larc.nasa.gov/>.

This research was primarily supported by the NASA ESPCOR CAN project.

## ABSTRACT

Past, current, and future climates have been simulated by the National Aeronautics and Space Administration (NASA) Goddard Institute for Space Studies (GISS) ModelE Global Circulation Model (GCM) and summarized by the Intergovernmental Panel on Climate Change Fourth Assessment Report (IPCC, AR4). New simulations from the updated CMIP5 version of the NASA GISS ModelE GCM were recently released to the public community during the summer of 2011 and will be included in the upcoming IPCC AR5 ensemble of simulations. Due to the recent nature of these simulations, they have not yet been extensively validated against observations. To assess the NASA GISS-E2-R GCM, model simulated clouds and cloud properties are compared to observational cloud properties derived from the Clouds and Earth's Radiant Energy System (CERES) project using MODerate Resolution Imaging Spectroradiometer (MODIS) data for the period of March 2000 through December 2005.

Over the 6-year period, the global average modeled cloud fractions are within 1% of observations. However, further study however shows large regional biases between the GCM simulations and CERES-MODIS observations. The southern mid-latitudes (SML) were chosen as a focus region due to model errors across multiple GCMs within the recent phase 5 of the Coupled Model Intercomparison Project (CMIP5). Over the SML, the GISS GCM undersimulates total cloud fraction over 20%, but oversimulates total water path by  $2 \text{ g m}^{-2}$ . Simulated vertical cloud distributions over the SML when compared to both CERES-MODIS and CloudSat/CALIPSO observations show a drastic

undersimulation of low level clouds by the GISS GCM, but higher fractions of thicker clouds.

To assess the impact of GISS simulated clouds on the TOA radiation budgets, the modeled TOA radiation budgets are compared to CERES EBAF observations. Because modeled low-level cloud fraction is much lower than observed over the SML, modeled reflected shortwave (SW) flux at the TOA is  $13 \text{ W m}^{-2}$  lower and outgoing longwave radiation (OLR) is  $3 \text{ W m}^{-2}$  higher than observations.

Finally, cloud radiative effects (CRE) are calculated and compared with observations to fully assess the impact of clouds on the TOA radiation budgets. The difference in clear-sky reflected SW flux between model and observation is only  $+4 \text{ W m}^{-2}$  while the  $\text{CRE}_{\text{SW}}$  difference is up to  $17 \text{ W m}^{-2}$ , indicating that most of the bias in  $\text{CRE}_{\text{SW}}$  results from the all-sky bias between the model and observation. A sizeable negative bias of  $10 \text{ W m}^{-2}$  in simulated clear-sky OLR has been found due to a dry bias in calculating observed clear-sky OLR and lack of upper-level water vapor at the 100-mb level in the model. The dry bias impacts  $\text{CRE}_{\text{LW}}$ , with the model undersimulating by  $13 \text{ W m}^{-2}$ . The  $\text{CRE}_{\text{NET}}$  difference is only  $5 \text{ W m}^{-2}$  due to the cancellation of SW and LW CRE biases.

## CHAPTER I

### INTRODUCTION

The world continues to industrialize and modernize, resulting in increased CO<sub>2</sub> emissions, and causing global climate change to become a major concern. Many studies have shown that a steady increase in surface temperature has occurred globally over the past few decades (Hansen et al. 2006). Various institutes around the world have developed global circulation models (GCMs) in order to predict the impact current CO<sub>2</sub> emissions, and other scenarios of increased CO<sub>2</sub> emissions such as double or quadruple CO<sub>2</sub>, have on the atmosphere. These GCMs attempt to simulate past and present climate, and to predict future climates.

Clouds and cloud feedbacks play important roles in the global radiation energy budget, but it is uncertain how clouds and their feedbacks evolve over time. Numerous studies throughout the years have indicated that cloud feedbacks are a major source of uncertainty in climate sensitivity and predicting climate change amongst the GCMs (Cess et al. 1989; Houghton et al 2001; Stephens 2005, Bony et al. 2006; Randall et al. 2007). These studies have partially motivated the following projects/programs: the Coupled Model Intercomparison Project (CMIP), the Program for Climate Model Diagnosis and Intercomparison (PCMDI), and the Intergovernmental Panel on Climate Change (IPCC) and their Assessment Reports (AR).

The IPCC was established in 1988 by the United Nations Environment Programme and the World Meteorological Organization, and its purpose is to “provide



the world with a clear scientific view on the current state of knowledge in climate change and its potential environmental and socio-economic impacts,” as defined by the IPCC (<http://www.ipcc.ch/>). In 1990, the IPCC released its first assessment report (FAR) detailing their first assessment of the atmosphere and climate change. The IPCC has periodically released assessment reports using available GCMs in an effort to better predict future climate scenarios due to global warming: Second assessment report (SAR, 1995), third assessment report (TAR, 2001), fourth assessment report (AR4, 2007), and an upcoming fifth assessment report to be released in 2014 using the current GCMs (AR5). Most of these reports have consisted of three working group reports followed by a synthesis report, which provides scientific information for decision and policy makers around the world.

In order to develop a standard experimental protocol for studying the output of coupled atmosphere-ocean GCMs, CMIP was established in 1995 under the World Climate Research Programme and the Working Group on Coupled Modeling. CMIP is essentially a framework designed to support climate model diagnosis, validation, intercomparison, documentation, and data access (<http://cmip-pcmdi.llnl.gov/cmip5/>). Phase three of CMIP (CMIP3) provided much of the data used within the IPCC AR4. As the IPCC prepares for AR5, model runs are being output to CMIP5 for public use.

While GCMs are the best tool for predicting the future climate change and its impacts, GCMs have limitations. As outlined in Lin et al. (2007), many models during AR4 were plagued with a double-intertropical convergence zone (ITCZ). The double-ITCZ still exists within many of the GCM results being prepared for AR5, and it is known to cause issues with excessive tropical precipitation, sensitivity of precipitation to

sea-surface temperature (SST), sensitivity of surface air humidity to SST, insufficient sensitivity of cloud amount to precipitation, and insufficient sensitivity of stratus cloud amount to SST. In terms of cloud cover, the double ITCZ results in thicker modeled ITCZ cloud band than seen in observations. A study by Karlsson et al. (2008) showed that the nine GCMs in AR4 also undersimulated low-level subtropical marine stratocumulus clouds compared to the international satellite cloud climatology project (ISCCP) D2 VIS/IR observations. Marine stratocumulus cloud simulations continue to be an issue within many models for AR5.

Past, current, and future climates have been simulated by the National Aeronautics and Space Administration (NASA) Goddard Institute for Space Studies (GISS) ModelE GCM and summarized by IPCC AR4. New simulations from the updated CMIP5 version of the NASA GISS ModelE GCM were recently released to the public community during the summer of 2011 and will be included in the IPCC AR5 ensemble of simulations. Due to the recent nature of these simulations, changes made to the GCMs since the previous assessment report have yet to be extensively validated against observations.

The Clouds and Earth's Radiant Energy System (CERES) project was created to monitor changes in the earth's radiant energy system and cloud systems, and to examine the critical cloud/climate feedback mechanisms that may play a major role in determining future changes in the climate system (Wielicki et al. 1996). The first CERES instruments were launched aboard the Tropical Rainfall Measuring Mission (TRMM) in November 1997 and on the Earth Observing System (EOS) Terra satellite in December of 1999.

CERES joined in the NASA Afternoon Constellation, or A-Train, later in 2002 aboard the EOS satellite Aqua (Stephens et al. 2002).

The Cloud-Aerosol Lidar and Infrared Pathfinder Satellite Observation (CALIPSO) mission was launched in April 2006 along with the CloudSat satellite as part of the A-Train constellation (Winker et al. 2007). CALIPSO carries CALIOP, a nadir viewing two-wavelength (1064 nm and 532 nm) polarization lidar, which is the first polarization lidar in space. CloudSat carries the first spaceborne millimeter wavelength cloud radar, giving it the unique ability to observe jointly most of the cloud condensate and precipitation within its nadir field of view and provide profiles of these properties with a vertical resolution of 500 m (Stephens et al. 2002). CALIPSO and CloudSat together provided a complete vertical cloud profile. A battery anomaly occurred on the CloudSat satellite on April 17<sup>th</sup>, 2011, causing the satellite to cease collecting data and lost formation with the A-Train. CloudSat has resumed to the A-Train on May 15<sup>th</sup>, 2012, and now flies 100 seconds behind CALIPSO.

This study presents a comparison of NASA GISS-E2-R simulated clouds and Top-Of-Atmosphere (TOA) radiation budgets against multiple observational datasets. Modeled cloud areal fractions and total water path are compared with SYN1 results retrieved from the MODerate resolution Imaging Spectroradiometer (MODIS) observations by the CERES science team (hereafter CERES-MODIS), while modeled vertical distributions of clouds are compared with the combined observations of CALIPSO-CloudSat. Simulated TOA radiation budgets are compared with CERES EBAF observations. Because of the ongoing issue with marine stratocumulus clouds in multiple CMIP5 simulations, particularly simulation of the southern mid-latitude storm

tracks, this study will focus on clouds and their impact on the TOA radiation budgets over the southern mid-latitude oceans.

## CHAPTER II

### DATA SETS

In this study, GISS-E2-R global circulation model (GCM) Atmospheric Model Intercomparison Program (AMIP) and historical simulations are compared to CERES-MODIS SYN1/EBAF and CloudSat/CALIPSO observations. These datasets are discussed in detail below.

#### CMIP5 GISS-E2-R GCM Model Data

Monthly and daily simulated GISS-E2-R runs were retrieved using the Earth System Grid Federation (ESGF) Program for Climate Model Diagnosis and Intercomparison (PCMDI) database at a horizontal resolution of  $2^{\circ} \times 2.5^{\circ}$  (latitude x longitude).

Multiple simulations of each model are provided by the ESGF PCMDI database. Each ensemble member is given three integers (N,M,L) in the  $r\langle N \rangle_i \langle M \rangle_p \langle L \rangle$  format to distinguish related simulations as detailed in Taylor et al. (2011), where N is the realization number, M is the initialization method indicator, and L is the perturbed physics number. The realization number distinguishes which set of initial conditions are used, and for this study, only the fifth realization will be used. Initial research showed negligible difference globally between realizations. Only one initialization method, M, was available for the GISS GCM at the time of this study. The third version of perturbed physics is used for this study to allow the physics scheme to include aerosol effects in the

model. Thus, the r5i1p3 ensemble member was chosen for this study and used for all variables and for both AMIP and historical simulations to ensure consistency.

#### *AMIP versus Historical Runs*

AMIP runs of the GISS GCM are primarily used in this study for global and regional TOA comparisons. The benefit of using AMIP runs as opposed to historical runs is that sea surface temperature (SST) and sea ice are prescribed, which helps to eliminate model and surface coupling biases for intercomparing models within CMIP5.

#### *Daily ISCCP Simulated Runs*

Daily runs of the GISS GCM are provided by the ESG PCMDI database using an ISCCP simulator. These runs are used to compare simulated cloud vertical profiles between the GCM and CERES-MODIS SYN1 observations. The benefit in using ISCCP simulated runs is that cloud fraction is split into a 7x7 grid for different types of clouds based on their optical depth and cloud-top pressure.

#### *Satellite Data*

For this study, satellite retrieved results are considered as truth during the comparison, although the satellite retrievals are not perfect and need to be validated as shown in other studies (Dong et al. 2008; Giannecchini et al. 2013). Satellite observations and retrievals are however becoming more accurate over time and as such are the best option for in-depth comparison to assess model accuracy.

#### *CERES-MODIS*

This study uses two CERES-MODIS datasets for global and regional comparisons at TOA (Loeb et al. 2009). These datasets are derived from four CERES instruments housed by two satellites; FM1 and FM2 aboard Terra, FM3 and FM4 aboard Aqua.

These satellites are part of National Aeronautics and Space Administration's (NASA's) Earth Observing System (EOS), created to study the Earth and its changing environment. Both satellites have sun-synchronous near-polar orbits, and operate at an altitude of 705 km. Terra launched in December of 1999 and crosses over the equator at 10:30 AM local standard time. Aqua launched on May 4<sup>th</sup>, 2002, and was the first satellite to make up the Afternoon Constellation (A-Train) satellites (Stephens et al. 2002). Aqua crosses over the equator at 1:30 PM local standard time with a repeat cycle of 16 days (Winker et al. 2007).

A major uncertainty in CERES-MODIS observations occurs over the Arctic regions, particularly during cold seasons, making a comparison over the Arctic highly questionable in this study. The CERES-MODIS instruments aboard Aqua and Terra have difficulty differentiating cloud layers and the ice covered sea-surface below due to the limitation of passive remote sensing. This limitation causes cloud fractions, cloud properties, and clear-sky fluxes over the arctic region to be highly questionable. As shown and concluded in Giannecchini et al. (2013), passive CERES-MODIS retrieved CFs agree well with those from CC and Atmospheric Radiation Measurement (ARM) during warm months, but CERES Ed2 polar-cloud detection algorithms have trouble distinguishing thin clouds from cold surface temperatures present during winter when only infrared data can be used.

#### *CERES-MODIS : SYN1*

Terra and Aqua retrieved radiances are processed by NASA CERES Science team and converted to flux measurements through the use of scene IDs and angular directional models (ADMs) to create level 2 Single Scanner Footprint TOA/Surface Fluxes and

Clouds (SSF) data. These footprints are then placed into a  $1.0^{\circ} \times 1.0^{\circ}$  grid to create the CERES SSF1deg\_Hour dataset. With the help of geostationary satellite observations, the diurnal cycle is inferred and used to create the SYN1 (Synoptic Radiative Fluxes and Clouds) dataset. This dataset will be used in this study as observational truth for gridded cloud fraction, total water path, and optical depth comparisons (CERES-MODIS). For TOA radiation budget comparisons, CERES EBAF-TOA data will be used.

*CERES-MODIS : EBAF-TOA (EBAF)*

While SYN1 TOA radiation data are available for comparison with GCM results, a more refined and accurate data product is also available, the CERES Energy Balanced and Filled at TOA (EBAF-TOA, hereafter EBAF) data product, which is derived from SYN1 results and is specifically designed for climate modelers who need a net imbalance constrained to the ocean heat storage term. CERES achieves this by balancing TOA fluxes to reach a net balance and spatially filling clear-sky missing data holes (look into adding this Hansen et al 2005 reference). To reach TOA net balance, SYN1 TOA fluxes are balanced within their uncertainties, with the largest uncertainties of 2% and 1% occurring in the shortwave and longwave, respectively. Filling in areas of missing SYN1 data is imperative for clear-sky and arctic comparisons, otherwise global values become drastically skewed by monthly data where no clear-sky samples were observed. In detail, CERES EBAF data will be used for GCM comparison of all-sky and clear-sky reflected/absorbed shortwave radiation, all-sky and clear-sky outgoing longwave radiation, and for all-sky net flux. All-sky and clear-sky results will also be used to calculate shortwave, longwave, and net cloud radiative effects.



*CloudSat/CALIPSO (CC)*

Because passive sensors only see the top layer of a cloud, using the active sensors from CloudSat/CALIPSO will provide a more accurate assessment of observed vertical cloud profiles. CC observed vertical profiles of clouds from July 2006 through June 2010 are compared with GISS simulated cloud vertical profiles over the SML in this study.

CHAPTER III  
METHODOLOGY

Statistical Methods, Spatial Degradation, and Degradation Sensitivity

*Statistical Methods*

In order to properly assess the GISS GCM and its sensitivities, a few basic statistical methods are employed and presented in Table 1. Global averages are computed through the following two steps (temporal average first, and then spatial). First, the monthly averages (for example January) are binned and averaged from all monthly means (for all Januaries from 2000-2005) for a grid box, and then the seasonal and annual averages are calculated from the averages from January to December. Once the monthly, seasonal and annual averages over a grid box are created, a global mean is computed using a cosine weighting scheme, where the weight applied to each datum is the cosine of the latitude to which that datum belongs. After dividing by the sum of the weights, a global cosine weighted mean is achieved.

Table 1. Basic statistics used for calculating the weighted mean bias, standard deviation, and correlation between the GCM and observations.

Statistic	Equation
Mean	$\bar{x} = \frac{1}{N} \sum_{i=1}^N x_i$

Table 1. (Cont.)

Weight	$w = \cos(\text{latitude})$
Weighted Mean	$\bar{x} = \frac{\sum_{i=1}^N w_i x_i}{\sum_{i=1}^N w_i}$
Standard Deviation	$\sigma_N = \sqrt{\frac{1}{N-1} \sum_{i=1}^N (x_i - \bar{x})^2}$
Covariance	$Cov(X, Y) = \sum_{i=1}^N \frac{(X_i - \bar{X})(Y_i - \bar{Y})}{(N-1)}$
Correlation	$Corr(X, Y) = \frac{Cov(X, Y)}{\sigma_X \sigma_Y}$

### *Spatial Degradation*

This study employs the use of spatial degradation to alleviate the problem of comparing datasets of differing spatial resolutions. The result of this spatial degradation is the coarsening of 1°x1° CERES-MODIS gridded data to match the 2°x2.5° gridded resolution of the GISS GCM. A new 2°x2.5° grid for CERES-MODIS data is initialized and then populated using bilinear interpolation as given in Equation 1.

$$\begin{aligned}
 f(x, y) = & \frac{1}{(x_2 - x_1)(y_2 - y_1)} ( f(x_1, y_1)(x_2 - x)(y_2 - y) + f(x_2, y_1)(x - x_1)(y_2 - y) \\
 & + f(x_1, y_2)(x_2 - x)(y - y_1) + f(x_2, y_2)(x - x_1)(y - y_1) ) \quad (1)
 \end{aligned}$$

### *Degradation Sensitivity*

Because data interpolation has the potential to modify the original data, a sensitivity study has been conducted to demonstrate that the change before and after data interpolation is minimal and irrelevant to this study. Results (see Table 2) show minimal change in global averages due to spatial degradation by bilinear interpolation. Since these changes are well within the range of uncertainty, global alterations in the data due to bilinear interpolation can be considered negligible. Standard deviations were expected to decrease slightly due to this filtering and actually decreased by a small margin for most parameters. Only the standard deviation in net flux at TOA increased slightly after applying bilinear interpolation.

Table 2. Sensitivity study showing global average and standard deviation of SYN1 and EBAF data, before and after, spatial degradation through interpolation.

Variable & Units		Pre-Interpolation EBAF/SYN Global Average	Post-Interpolation EBAF/SYN Global Average	Pre-Interpolation EBAF/SYN Std. Deviation	Post-Interpolation EBAF/SYN Std. Deviation
Cloud Fraction	[%]	61.57	61.54	15.38	15.33
TWP	[ $g\ m^{-2}$ ]	118.45	118.33	73.80	73.42
SW $\uparrow$ TOA	[ $W\ m^{-2}$ ]	99.73	99.68	17.13	17.01
SW( $\downarrow\uparrow$ ) TOA	[ $W\ m^{-2}$ ]	240.58	240.61	96.39	96.32
LW $\uparrow$ TOA	[ $W\ m^{-2}$ ]	239.78	239.84	36.59	36.37
Net Flux TOA	[ $W\ m^{-2}$ ]	0.79	0.76	64.73	64.85
C_SW $\uparrow$ TOA	[ $W\ m^{-2}$ ]	52.43	52.42	29.67	29.51
SW CRE	[ $W\ m^{-2}$ ]	-47.30	-47.27	23.98	23.91
C_LW $\uparrow$ TOA	[ $W\ m^{-2}$ ]	266.12	266.17	42.03	41.77
LW CRE	[ $W\ m^{-2}$ ]	26.33	26.33	12.08	12.05
Net CRE	[ $W\ m^{-2}$ ]	-20.96	-20.94	16.12	16.04

A sensitivity analysis was also conducted over the main focus region, the Southern Mid-Latitudes. Most results showed again minimal changes to both regional average and standard deviation, and can be found in Table 3. A change of  $2 \text{ W m}^{-2}$  is however noted in absorbed SW radiation, and is hypothesized to be due to bilinear interpolation including data from a latitudinal band closer to the equator, where values of absorbed shortwave radiation are higher. Sensitivity studies over the SMLs showed another interesting result, in that many standard deviations actually increased after filtering through bilinear interpolation rather than decreasing as expected.

Table 3. Sensitivity study showing the average and standard deviation of SYN1 and EBAF data, before and after, spatial degradation through interpolation over the southern mid-latitudes.

Variable & Units		Pre-Interpolation EBAF/SYN SML Average	Post-Interpolation EBAF/SYN SML Average	Pre-Interpolation EBAF/SYN Std. Deviation	Post-Interpolation EBAF/SYN Std. Deviation
Cloud Fraction	[%]	78.95	78.63	6.89	7.00
TWP	$[g \text{ m}^{-2}]$	200.24	198.76	46.41	47.45
SW $\uparrow$ TOA	$[W \text{ m}^{-2}]$	105.11	104.86	6.80	6.96
SW( $\downarrow\uparrow$ ) TOA	$[W \text{ m}^{-2}]$	202.30	204.65	44.33	44.31
LW $\downarrow$ TOA	$[W \text{ m}^{-2}]$	227.45	228.24	15.81	15.95
Net Flux TOA	$[W \text{ m}^{-2}]$	-25.15	-23.59	29.71	29.63
C_SW TOA	$[W \text{ m}^{-2}]$	37.75	37.67	3.29	2.89
SW CRE	$[W \text{ m}^{-2}]$	-67.35	-67.20	7.04	7.22
C_LW TOA	$[W \text{ m}^{-2}]$	257.96	258.74	15.22	15.09
LW CRE	$[W \text{ m}^{-2}]$	30.51	30.50	4.46	4.60
Net CRE	$[W \text{ m}^{-2}]$	-36.84	-36.70	6.31	6.45

### *Region of Interest*

Regions that constitute the SML for this study are outlined in Figure 1. Specifically, the boundaries for the left and right region are confined within 30°S to 62°S latitude, and between 43°E to 110°E and 182°E to 270°E longitude, respectively. These boundaries were chosen because: (1) they contain significant differences in cloud fraction between the model simulations and observations (2) they contain a high frequency of marine boundary layer (MBL) clouds which GCMs have difficulty simulating, and (3) they are located away from land and shorelines, which eliminates land effects.

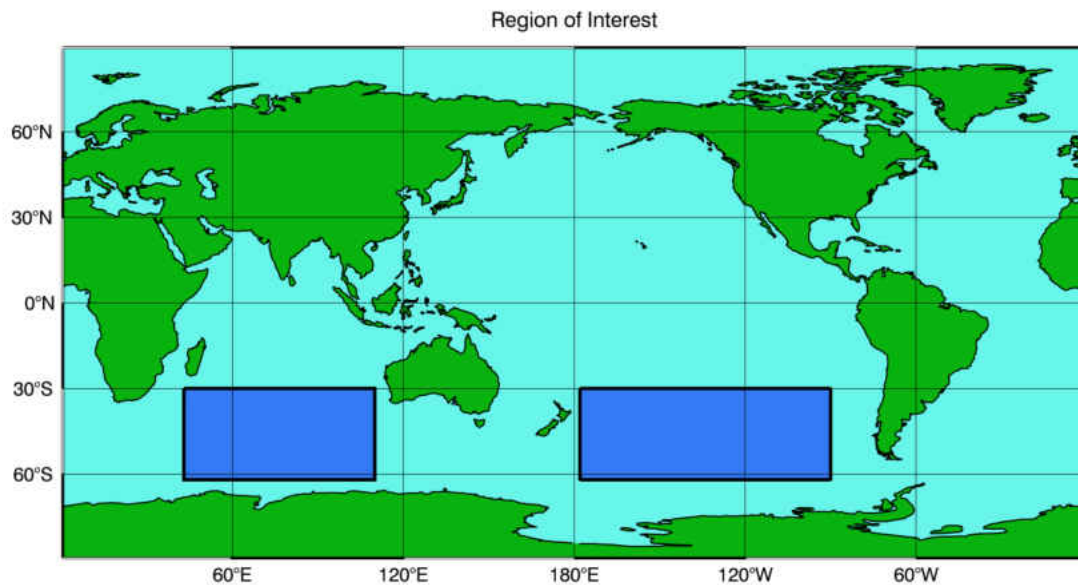


Figure 1. Dark blue polygons outline regions used in SML comparisons.

## CHAPTER IV

### RESULTS AND DISCUSSION

#### PART 1: Comparison of Cloud Properties

Cloud property comparisons have been conducted both globally and regionally over the southern mid-latitude storm track. Cloud fraction, total water path, and optical depths from GISS-E2-R (GISS) simulations are compared to CERES-MODIS observations over the time period of March 2000 to December 2005. GISS GCM vertical cloud fraction profiles are compared to CloudSat/CALIPSO radar-lidar active retrievals. Comparisons are conducted using yearly and seasonal data, namely southern hemisphere summer (December, January, and February; DJF) and southern hemisphere winter (June, July, and August; JJA), for all variables.

#### *Cloud Fraction (CF)*

To assess GISS simulated clouds and their impact on the radiation budget, this study examined the annual mean CFs and their global distributions for the GISS GCM (Figure 2a), the CERES-MODIS SYN1 observations (Figure 2b), and the difference between the two given as GISS-SYN1 (Figure 2c).

As shown in Figure 3, the overestimates CFs in polar regions, underestimates in the mid-latitudes, and overestimates in tropical regions. One reason for this may be how the model is tuned to reach radiative balance at TOA. For any model to be accepted within the Coupled Model Intercomparison Project (CMIP), the model must be in global

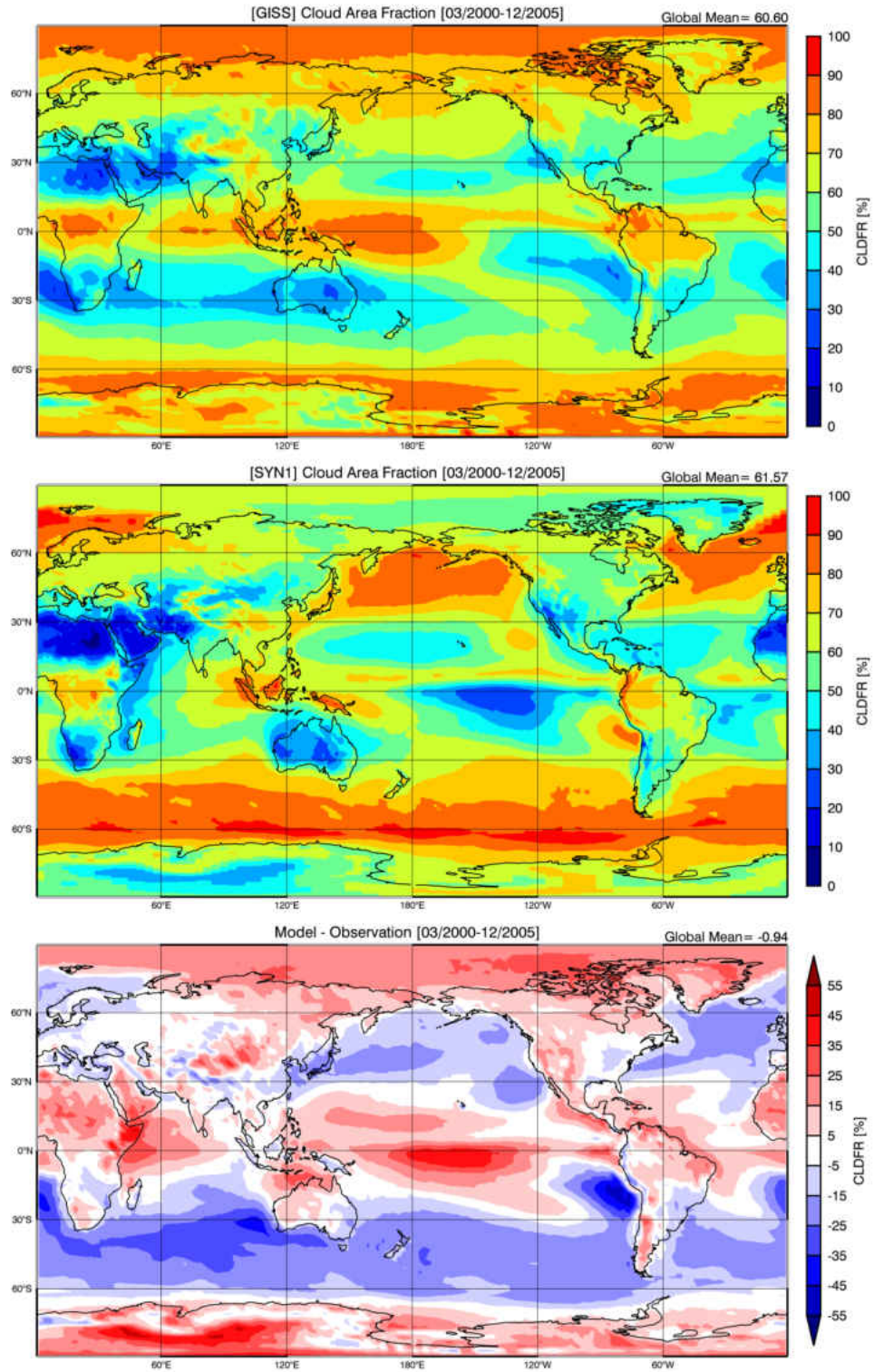


Figure 2. Gridded annual mean CAFs for the (a)GISS GCM, (b)SYN1 observations, and the difference (c)GISS – SYN1, for the period of March 2000 through December 2005.



radiative balance. NASA GISS achieves global radiative balance in the GCM by tuning the threshold value of humidity  $U_{00}$  at which clouds are formed (Schmidt et al. 2006). Of particular interest is the undersimulation of MBL clouds in the mid-latitudes. While this study will examine in detail the undersimulation of MBL over the SML, it is noted that the unsimulation of marine clouds in the northern mid-latitudes (NML) could be related to the issues that result in the undersimulation of SML MBL clouds. Figure 2 also shows that the simulated ITCZ is much wider than the observed ITCZ. This is common in most GCMs where a double ITCZ is actually produced, which makes the zone look much wider than it should be (Lin, 2007).

It should be pointed out that observations, while considered to be truth for this study, have relatively large uncertainties, particularly over some regions and during specific seasons. For example, CERES Ed.2 CFs agree well with Department of Energy (DOE) Atmospheric Radiation Measurement (ARM) and CC results during warm months (May-Oct.), but are significantly lower during cold months (Nov.-April) over Arctic regions (Giannecchini et al. 2013). Additionally, preliminary CERES Ed.4 results have shown a 7% global mean CF increase and a large increase in Arctic regions compared to the Ed.2 results (Minnis et al. at 10/2011 and 05/2012 NASA CERES ST meetings, available at <http://ceres.larc.nasa.gov/science-team-meetings2.php>).

While the global mean total column CF difference between the GISS GCM, 61%, and CERES-MODIS observations, 62%, is within 1%, large differences exist regionally as shown in Figure 2. It is hypothesized that the GCM can fairly accurately predict global clouds and their impacts on the global radiation budget; however large offsetting biases may exist regionally between the model and observations. As such, this study

assesses the regional cloud biases and the impacts of these cloud biases on their radiation budgets over the SML regions.

Over the SML, the CERES observed CF is 79% while modeled CF is 58%, a 21% underestimation. Observations show a band of high CFs due to the southern storm track clouds, and CF decreasing with latitude, while the GCM instead shows a steady increase of clouds with latitude.

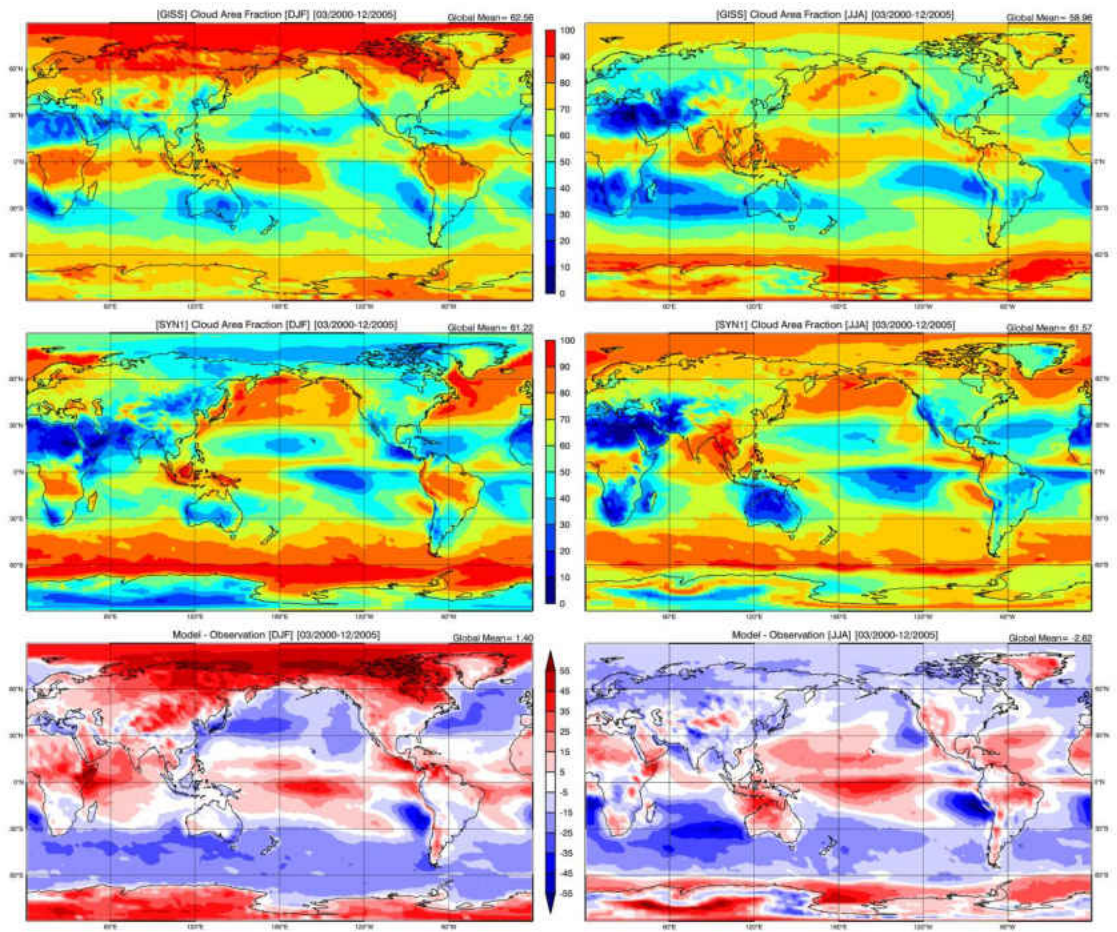


Figure 3. Same as Figure 2, except split seasonally into northern hemisphere winter (DJF, left) and summer (JJA, right).

Northern hemisphere winter (DJF, left) and summer (JJA, right) CF comparisons are shown in Figure 3. Seasonal global mean comparisons of CF between the model and

CERES-MODIS observations are close to one another during both seasons, with a small oversimulation of clouds during DJF (63 and 61%, respectively), and a small undersimulation of clouds during JJA (59 and 62%, respectively). The ITCZ in the GCM also remains quite wide for both seasons, suggesting that this issue is not seasonal, but year round. It is noticed that the simulated cloud fractions over the polar regions during each hemisphere winter are much higher than observations. This may particularly attribute from the limitation of observations where passive satellites have difficulty distinguishing clouds from highly reflective sea ice or snow, especially during polar night.

MBL clouds observed in both winter and summer seasons over mid-latitudes are missed by the GCM. However, CF amounts in the SML remain consistent during both the southern hemisphere winter and summer for both the GISS GCM and observations. The GISS GCM simulates CFs of 59 and 58% during the summer and winter, respectively, while observations show a steady CF of 78% during both seasons.

To assess how well the GCM simulates clouds vertically over the SML, model simulations are compared to observational results derived from the active sensor aboard CloudSat/CALIPSO and shown in Figure 4. Reasons for using this dataset are discussed previously in Chapter II.

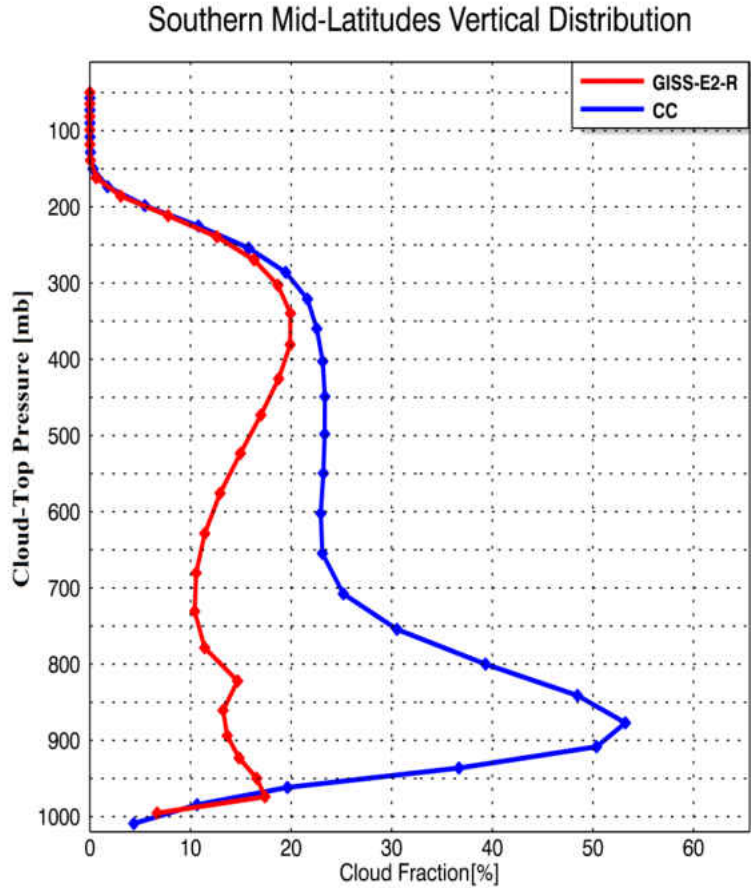


Figure 4. Vertical cloud fraction (%), as a function of cloud top pressure in millibars, for the GISS-E2-R GCM (red) over the period of March 2000 through December 2005 and for CloudSat/CALIPSO observations (CC, blue) over the period of July 2006 through June 2010.

As illustrated in Figure 4, the model drastically undersimulates low-level clouds below 700mb compared to CloudSat/CALIPSO observations, and moderately underestimates mid-level clouds between 300 and 700mb. The modeled peak just below 800mb is questionable and hypothesized to be due to the cutoff for the boundary layer within the model, where model dynamics and parameterizations change. Vertical cloud properties are explored further in the following sections, particularly when discussing optical depth.

### *Total Water Path (TWP)*

Comparisons of liquid and ice water path (LWP, IWP) between the GISS GCM and CERES-MODIS observations cannot be made at this time, due to the manner in which these variables are calculated. CERES-MODIS calculates LWP and IWP based on optical depth and particle size, be it liquid or ice particles, respectively. This essentially gives the LWP or IWP with a gridbox based only on cloudy pixels. LWP and IWP calculated by the GISS GCM however, is based on the mass of liquid/ice water within the column divided by the entire area of the column, cloudy and non-cloudy pixels alike. For a proper apple-to-apple comparison, LWP and IWP from CERES-MODIS observations must be multiplied by the liquid and ice cloud fraction, respectively. Liquid and ice cloud fractions are unavailable at this time for Edition 2 CERES-MODIS observations, and will not be available until Edition 4 results are released to the public.

Because of this, TWP will be compared between the model and observations in this section. TWP calculation methods are based on the data source. For the GISS GCM, TWP is calculated by adding IWP and LWP within a gridbox, and TWP is calculated for CERES-MODIS observations by adding LWP and IWP within a gridbox and then multiplying this value by the gridbox cloud fraction. The results of TWP calculations are shown in Figure 5.



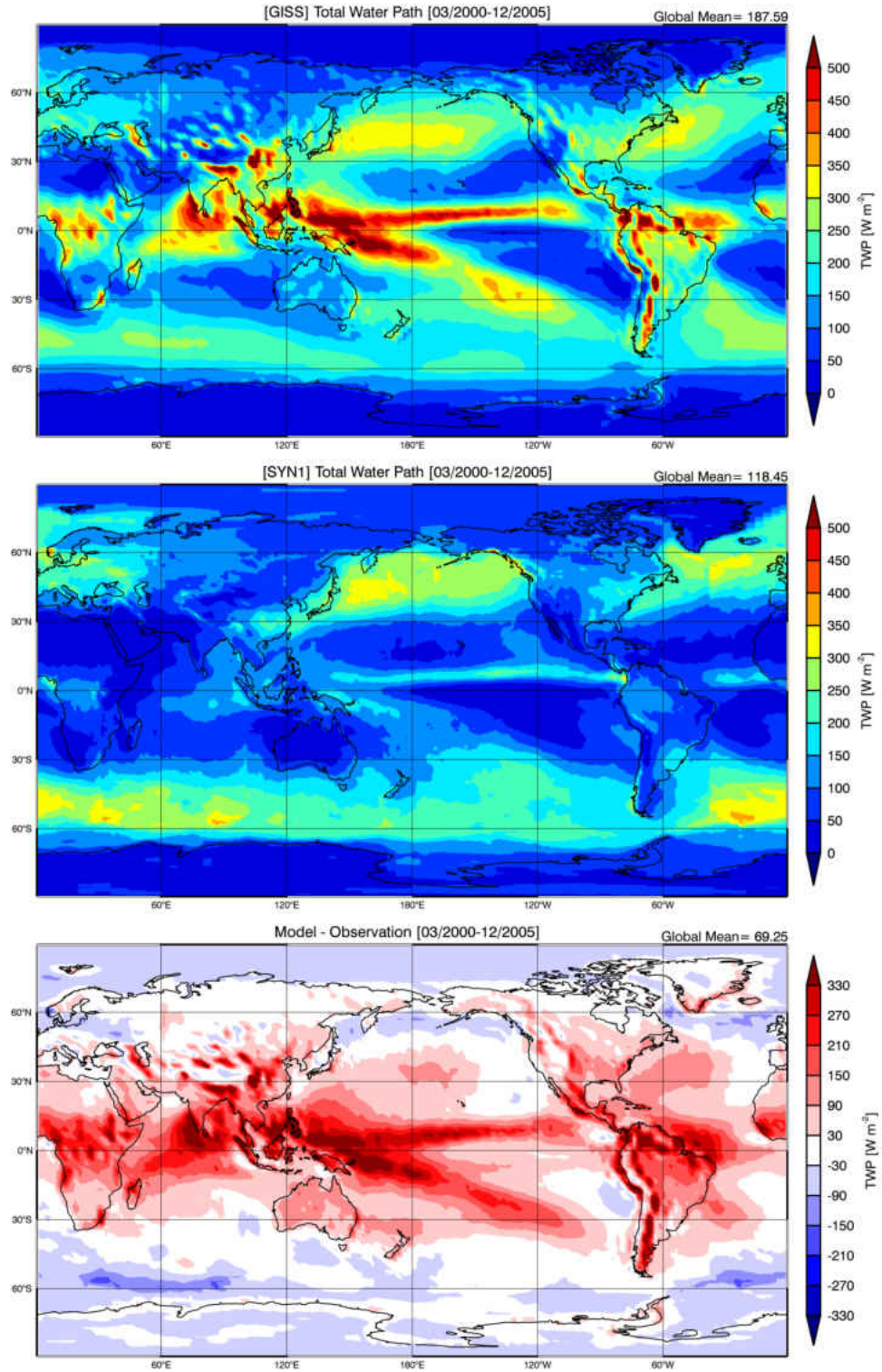


Figure 5. Total water path (TWP) of (a)GISS, (b)SYN1, and the difference (c)GISS – SYN1, for the period of March 2000 through December 2005.

Globally, the GISS GCM simulates TWP  $70 \text{ g/m}^2$  higher than observations (188 and  $118 \text{ g/m}^2$ , respectively). In particular, it is shown that the model strongly oversimulates TWP within tropical regions, and mostly undersimulates TWP in Arctic regions. However, regions exist within the tropics where TWP is undersimulated by the model due to the undersimulation of modeled clouds over these regions. This is hypothesized to be a result of the model undersimulating low-level marine stratocumulus.

Over the SML, the bias in TWP is around  $2 \text{ g/m}^2$ , with the model simulating  $202 \text{ g/m}^2$  and observations reporting  $200 \text{ g/m}^2$ . Considering that over the SML, TWP for the model and observations are nearly the same while modeled cloud fraction is undersimulated by  $> 20\%$ , fewer but thicker clouds are expected in the model compared to CERES-MODIS observations.

Figure 6 shows seasonal comparisons of TWP during winter and summer seasons. Biases shown in Figure 6c are fairly constant throughout the year, with modeled TWP oversimulation in tropical regions, and undersimulation in Arctic regions. The strongest biases in global mean TWP occur during JJA, when the model oversimulates TWP by  $77 \text{ g m}^{-2}$  compared to observations ( $193$  and  $116 \text{ g m}^{-2}$ , respectively), compared to an oversimulation of  $61 \text{ g m}^{-2}$  during DJF ( $183$  and  $121 \text{ g m}^{-2}$ , respectively).

Over the SML, the model oversimulates TWP by  $17 \text{ g m}^{-2}$  during the summer compared to observations ( $195$  and  $178 \text{ g m}^{-2}$ , respectively), while the model simulates TWP within  $3 \text{ g m}^{-2}$  during the winter ( $214$  and  $217 \text{ g m}^{-2}$ , respectively). Because seasonal CF variability proved negligible (differences within 1% for DJF and JJA), it is hypothesized that thicker clouds are being observed during JJA than during DJF, causing an increase in observed TWP during the winter.

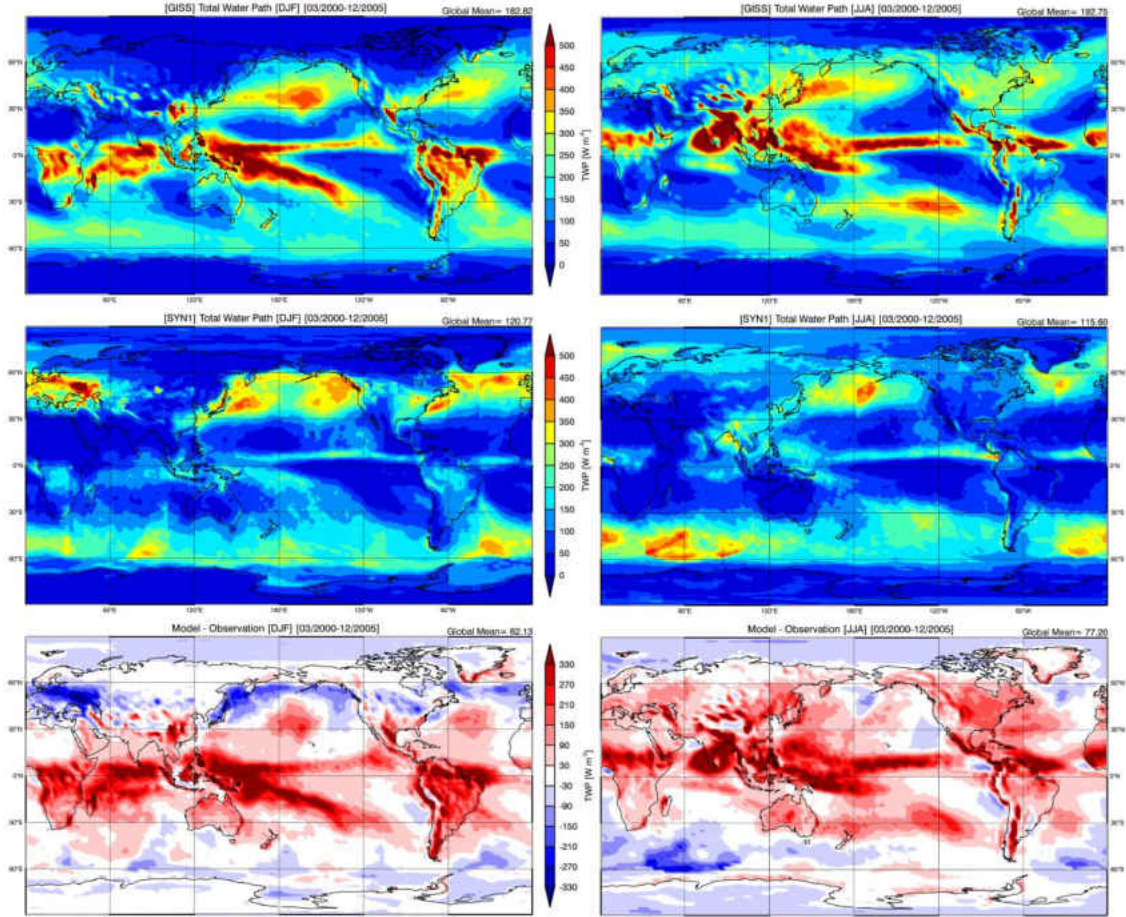


Figure 6. Same as Figure 5, except split seasonally into northern hemisphere winter (DJF, left) and summer (JJA, right).

### *Relationship of Cloud Fraction to Optical Depth*

Using daily SYN1 CERES-MODIS retrievals and ISSCP simulated GCM data over the SML, cloud fraction is stratified into a 7x7 and 6x7 grid by cloud optical thickness and cloud-top pressure in millibars for the model and observations, respectively, as shown in Figure 7. The farthest left column in the 7x7 modeled grid is cloud fractions with an optical depth between 0.02 and 0.3. Clouds of this optical depth cannot be seen by passive sensors, and as such will not be included in calculations and comparisons.



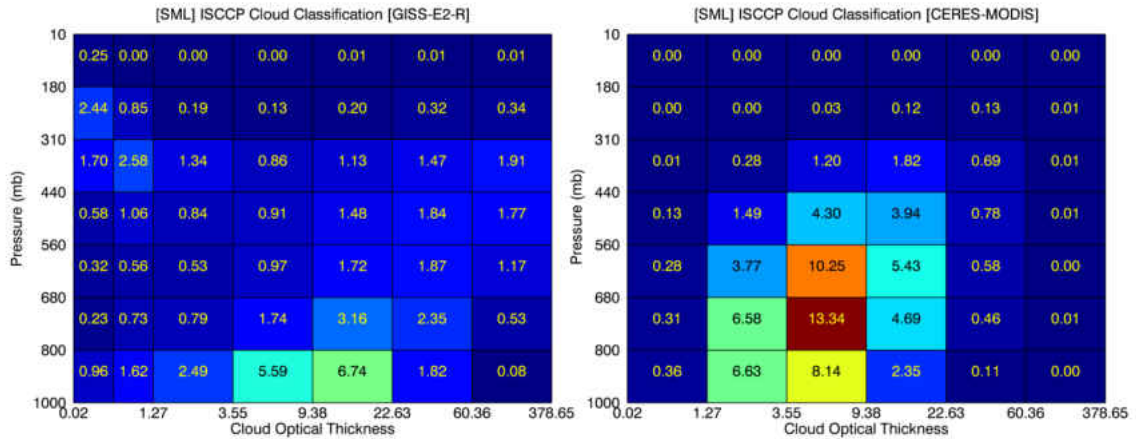


Figure 7. Classified cloud fractions based on both optical depth and cloud-top pressure for the GISS-E2-R GCM (left) and CERES-MODIS observations (right) over the SML.

Stratifying cloud fraction by optical thickness and cloud-top pressure confirms the results illustrated in Figure 4, that is, the GCM undersimulates the amount of lower-level clouds, lower than 680 mb, compared to CERES-MODIS and CloudSat/CALIPSO observations. Results also show that the model is grossly undersimulating the amount of mid-level clouds, 680-440 mb, and oversimulating high level clouds, <440 mb, compared to observations. This is hypothesized to occur due to attenuation and cloud height determination with passive sensors discussed following. Low-middle-high cloud level designations are based on previous studies (Zhang et al. 2005; Jin et al. 2006).

Figure 4 shows the greatest undersimulation of clouds to be across the lowest layer, 1000 to 800 mb. In Figure 7, however, the total cloud fraction within the lowest layer shows excellent agreement between the model and CERES-MODIS observations. This agreement is hypothesized to be a false positive result because CERES-MODIS observations see only the tops of clouds. This results in a positive cloud height bias, where a portion of the observed cloud fraction is moved upward from the lowest height classification layer.

It is also shown that the model oversimulates high-level cirrus clouds than found in observations. This may be the result of a negative cloud height bias in the observations. Since CERES-MODIS retrievals use effective temperature to determine cloud height, a portion of the thin upper-tropospheric cloud fraction is moved downward to a lower height classification layer (Xi et al. 2010).

While fewer clouds are present in the model, it is shown that model tends to have thicker clouds than found in observations, which is expected given that the model undersimulates total clouds in the SML by over 20%, while still maintaining equal amounts of TWP.

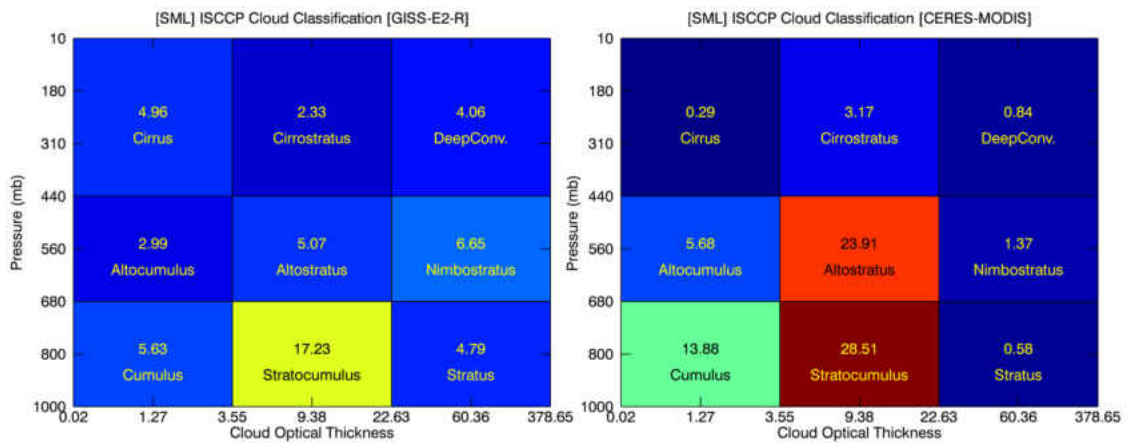


Figure 8. Same as Figure 7, except cloud classes are grouped into a 3x3 grid based on ISCCP Classifications used in Rossow and Shiffer (1999).

By grouping cloud types in Figure 7 to produce a simplified 3x3 grid as discussed in Rossow and Shiffer (1999), Figure 8 shows that model particularly underestimates altostratus, stratocumulus, and cumulus clouds in the atmosphere, but simulates higher percentages of thicker stratus, nimbostratus, deep convective clouds, and high-level cirrus when compared to CERES-MODIS observations.

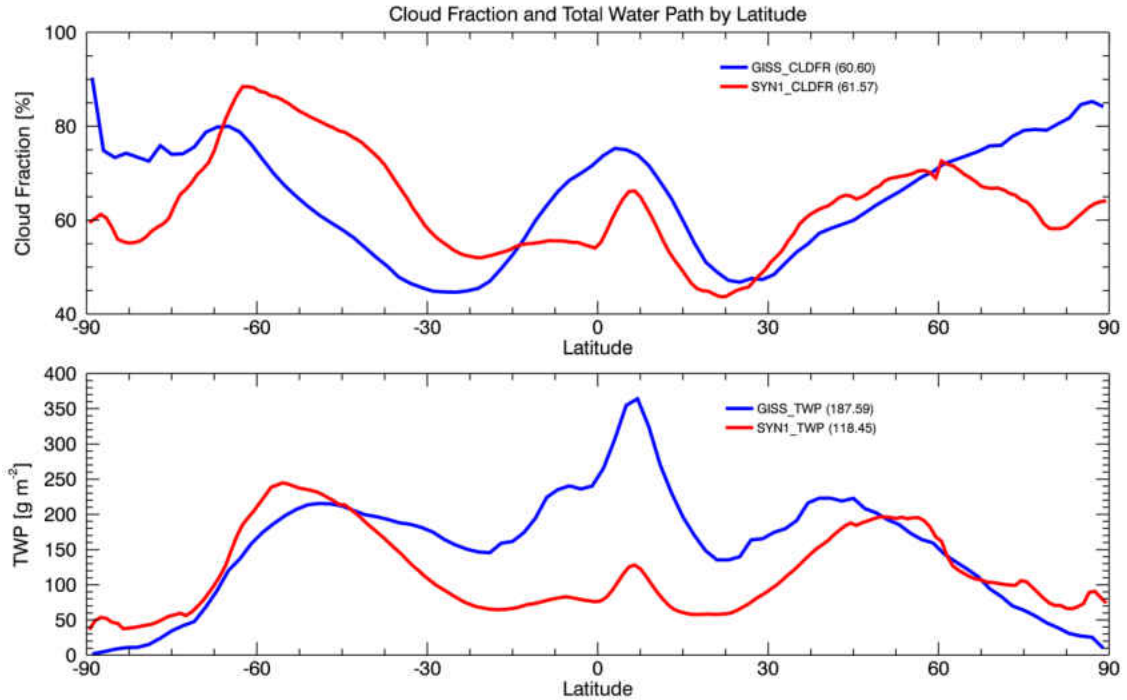


Figure 9. CF (top) and TWP (bottom) for the GISS GCM and CERES SYN1 results, averaged by latitude, over the period of March 2000 through December 2005.

Latitudinal averages of CF and TWP for the model and observations are shown in Figure 9, from south (left) to north (right). It is shown that while global CFs agree within 1%, large differences exist regionally between the model and observations. The greatest regional discrepancy in CF is seen in the SML. The pattern of oversimulation and undersimulation discussed previously is clearly seen in Figure 9, as well as the gross oversimulation of TWP by the GISS GCM globally. Close agreement between simulated and observed TWP is seen over the SML.

## PART 2: Impact of Clouds on the TOA Radiation Budget

This section examines the radiative effects of the global and regional cloud properties described in Part 1. Given that the GCM produces fewer but optically thicker low-level clouds than observations, it is expected that these cloud differences should

result in a significant negative bias in reflected shortwave (SW) at TOA due to cloud albedo effect. At the same time, the differences should have a minimal impact on outgoing longwave (LW) radiation (OLR) because low-level cloud top temperatures are close to sea-surface temperatures. To study in detail the radiative effects, modeled SW, LW and net fluxes at TOA are compared with CERES EBAF results. The all-sky TOA radiation fluxes discussed next will be combined with clear-sky radiative fluxes in Part 3 to investigate cloud radiative effects (CRE).

### *Shortwave Flux*

Figure 10 shows the modeled and observed reflected SW fluxes. When compared with CF in Figure 2, it is apparent that reflected SW flux generally increases with CF as expected, except for polar and desert regions, where surface albedos are nearly the same as cloud albedos. Modeled and observed global distribution patterns of CF and reflected SW flux are similar, in particular the CF and SW difference fields, which maintain the same sign except for within Arctic regions.

On global average, modeled reflected SW flux agrees with observed to within  $1 \text{ W m}^{-2}$  ( $101$  and  $100 \text{ W m}^{-2}$ ). However, large regional differences exist with a range of  $-40 \text{ W m}^{-2}$  near Peru to  $+40 \text{ W m}^{-2}$  over Indian Ocean. These regional biases closely resemble the bias pattern shown previously in CF: reflected SW fluxes in the mid-latitudes are underestimated while reflected SW flux over the polar and tropical regions are overestimated by the model. One major difference between CF and SW biases however, is that reflected SW in the Arctic is actually underestimated due to highly reflective sea-ice/snow surfaces. Regions of consistent marine stratocumulus clouds are underestimated by the GCM, due to the lack of clouds shown previously in CF results.

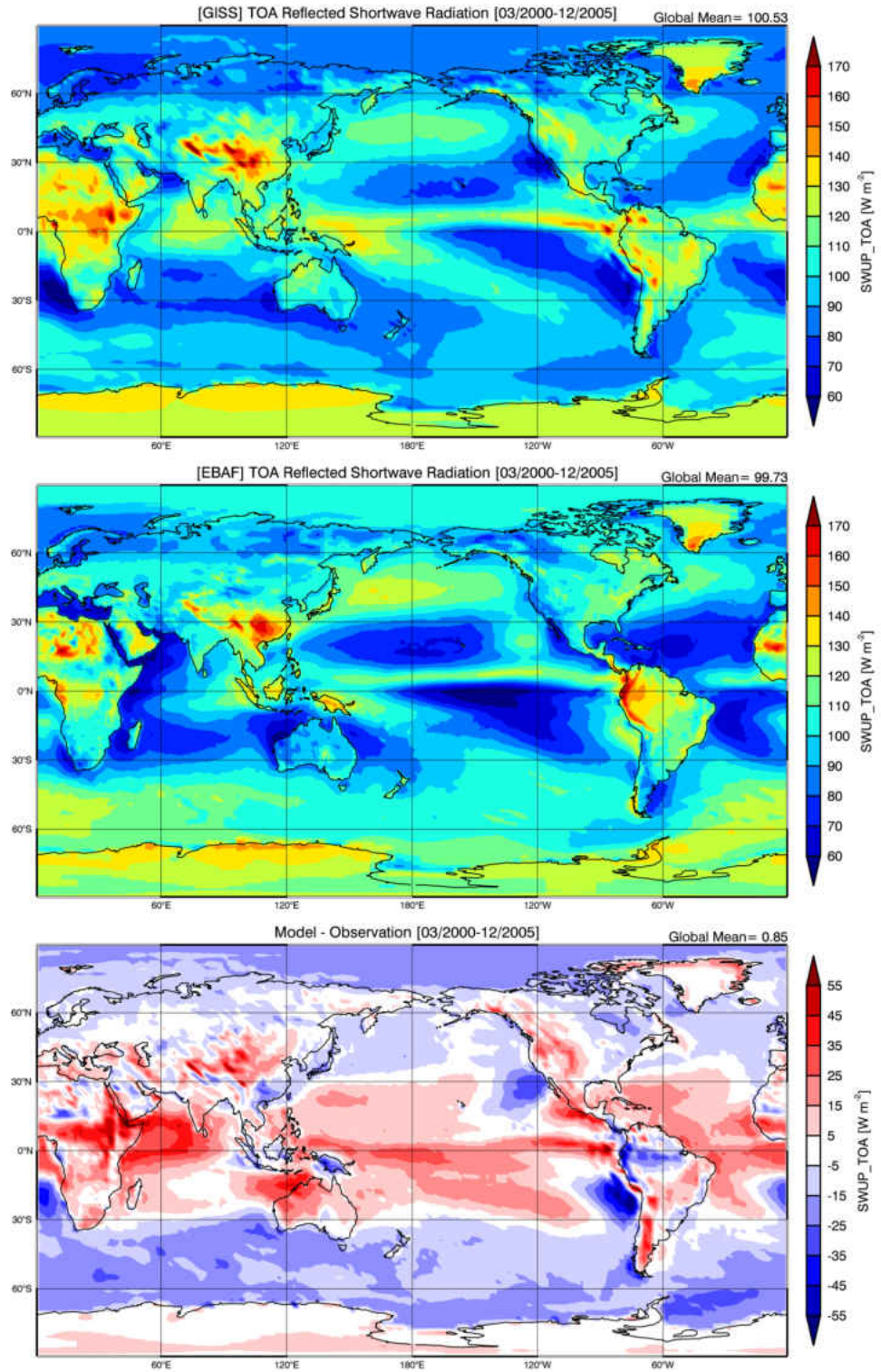


Figure 10. Reflected shortwave radiation at TOA for the (a)GISS GCM, (b)EBAF observations, and the difference (c)GISS – EBAF, for the period of March 2000 through December 2005.



In the SML, the modeled and observed reflected SW fluxes are  $92 \text{ W m}^{-2}$  and  $105 \text{ W m}^{-2}$ , respectively, which is an underestimation of  $13 \text{ W m}^{-2}$ . Comparing the  $13 \text{ W m}^{-2}$  negative bias in reflected SW with a 21% negative CF bias, the underestimation in SW flux is less than expected. The undersimulation in CF is compensated by oversimulation of cloud optical depth, resulting in a small difference in the reflected SW flux over the SML.

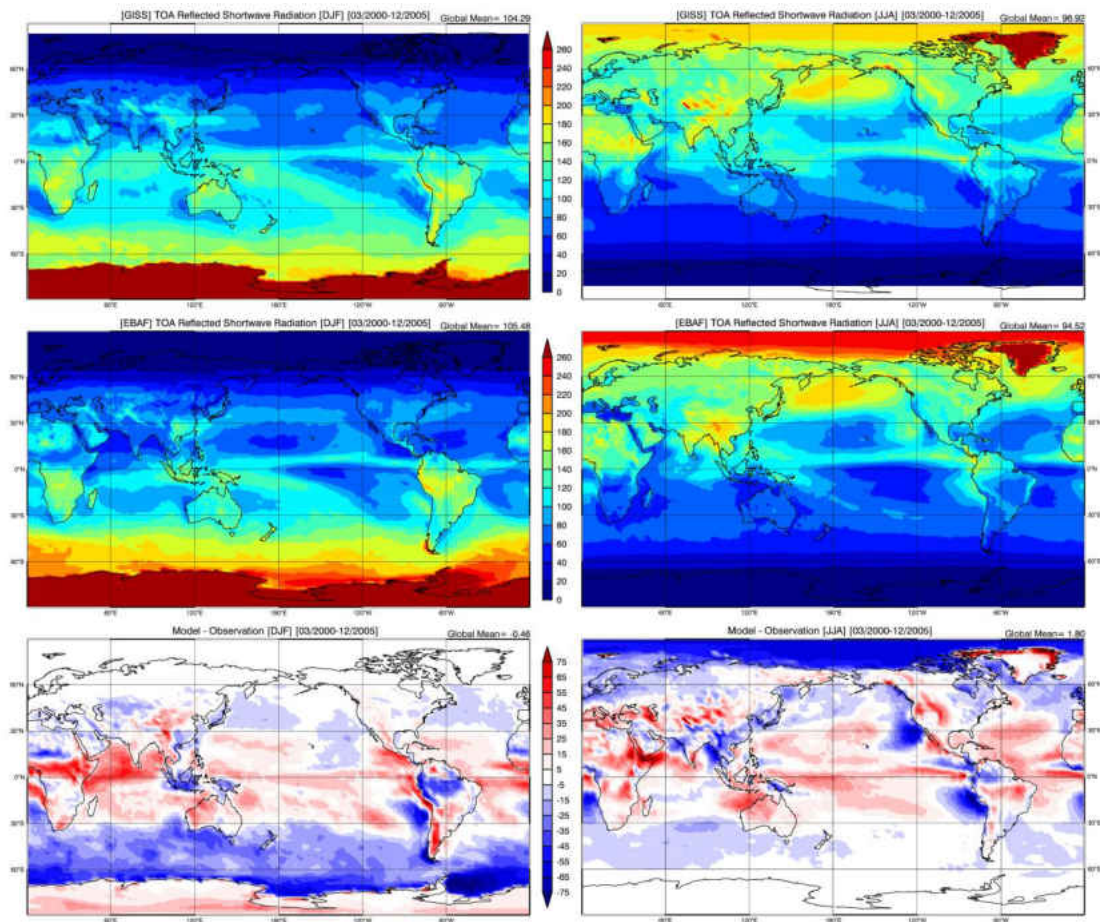


Figure 11. Same as Figure 10, except split seasonally into northern hemispheric winter (DJF, left) and summer (JJA, right).

For the seasonal comparisons, modeled global reflected SW fluxes have no shortwave bias during DJF, but contain a positive bias of  $2 \text{ W m}^{-2}$  during JJA. As in other comparisons, offsetting biases exist regionally in each season that when combined,

produce good agreement in the global average. For example, the difference can reach up to  $-70 \text{ W m}^{-2}$  over the Arctic during the summer season (JJA), due to a negative CF bias in the model simulation. A strong bias is found on the eastern coast of Greenland during JJA, where the GCM overestimates either the cloud amount or the albedo of the eastern Greenland mountain range. The same bias appears over the U.S. Rocky Mountains during summer as well; however, this overestimation appears to be directly correlated with the simulated cloud fraction over this region.

Stronger negative seasonal biases are found during DJF than during JJA over the SML ( $-20 \text{ W m}^{-2}$  and  $-4 \text{ W m}^{-2}$ , respectively), when a higher solar zenith angle causes more incident solar radiation to be received than during JJA. Since clouds have much higher albedos than the ocean, and cloud fraction is undersimulated over the SML, the modeled increase in reflected SW is less than the observed increase.

To further assess how GCM simulated shortwave flux compares with observations, absorbed shortwave radiation at TOA, computed using Equation 2, is shown in Figure 12. These results will be important in discussing the energy transfer between latitudes later in this chapter.

$$\textit{Absorbed SW} = (SW \downarrow - SW \uparrow) \quad (2)$$

As expected, global absorbed SW fluxes are inversely related to reflected SW fluxes shown in Figure 10. This is due to the nature of shortwave radiation, where if the incident SW radiation is constant at a given latitude, increasing reflected SW will decrease the amount of absorbed shortwave for a given latitude. That is, the regions where the model oversimulates/undersimulates reflected SW fluxes will certainly result in the undersimulation/oversimulation in absorbed SW radiation. Overall, the model has

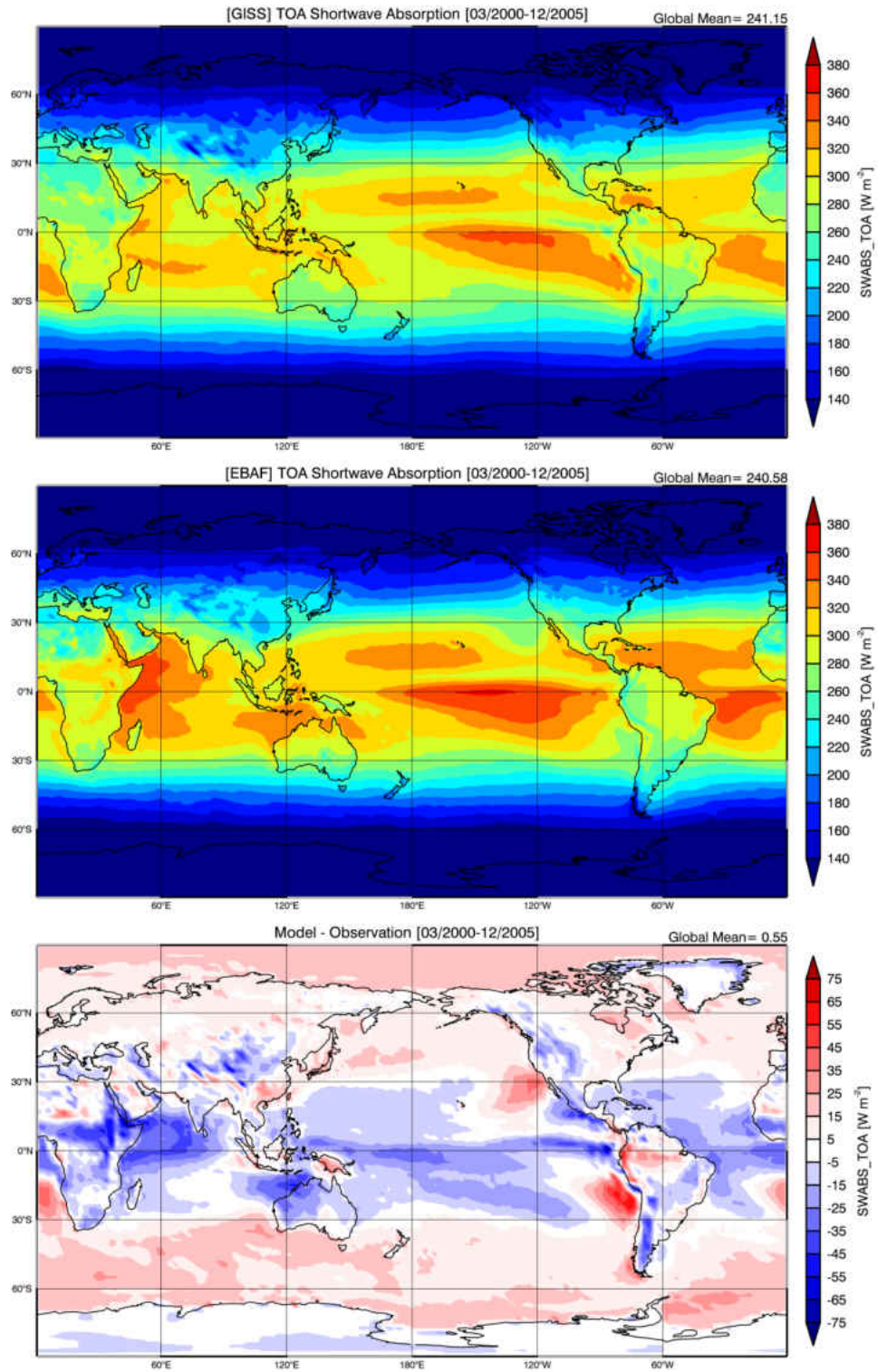


Figure 12. Absorbed SW radiation at TOA for the (a)GISS GCM, (b)EBAF observations, and the difference (c)GISS – EBAF, for the period of March 2000 through December 2005.



a global absorbed SW flux of  $241 \text{ W m}^{-2}$ , matching the observation.

Because modeled CF and therefore reflected SW fluxes are lower than observed over the SML, modeled absorbed SW radiation is higher than observed over this region. The modeled and observed absorbed SW fluxes over the SML are  $217 \text{ W m}^{-2}$  and  $202 \text{ W m}^{-2}$ , respectively, resulting in a positive bias of  $15 \text{ W m}^{-2}$ .

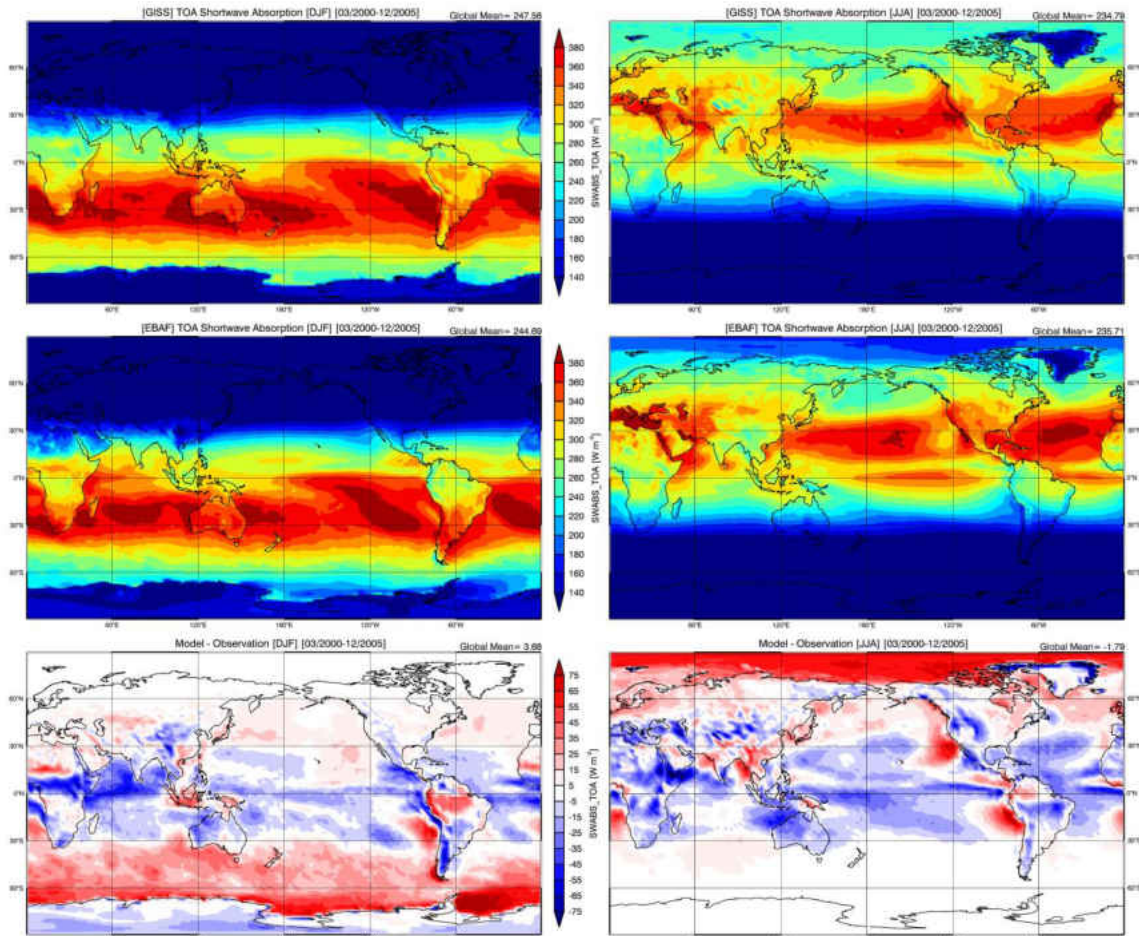


Figure 13. Same as Figure 12, except split seasonally into northern hemispheric winter (DJF, left) and summer (JJA, right).

As shown in Figure 15, seasonal absorbed shortwave flux patterns are essentially sun synchronous since each hemisphere receives more incident shortwave solar radiation during summer. Seasonal biases in absorbed SW flux essentially mirror reflective SW

biases, meaning large positive biases in absorbed SW flux correspond to large negative biases in reflected SW flux, such as over the SML and Arctic regions.

The model closely simulates mean global absorbed radiation during both DJF and JJA, with an oversimulation during DJF of  $3 \text{ W m}^{-2}$  (248 and  $245 \text{ W m}^{-2}$ ), and an undersimulation of only  $1 \text{ W m}^{-2}$  during JJA (235 and  $236 \text{ W m}^{-2}$ ). As discussed previously, regional model biases over the SML compared to observations are sun synchronous, with a minimal oversimulation of  $4 \text{ W m}^{-2}$  during the winter (98 and  $94 \text{ W m}^{-2}$ , respectively), and a gross oversimulation of  $33 \text{ W m}^{-2}$  during the summer (341 and  $318 \text{ W m}^{-2}$ , respectively).

#### *Longwave Flux*

To assess the impact of clouds on outgoing longwave radiation (OLR), gridded values of OLR at TOA are presented in Figure 14. OLR values, like SW fluxes, have a strong correlation with CF. Because cloud-top temperatures are generally much lower than the surface, particularly for high-level clouds, areas of higher CF emit less OLR than areas with little or no clouds.

Global distributions of OLRs simulated by the model and observed by CERES match each other at  $240 \text{ W m}^{-2}$ . Regional differences between the model and observations tend to be minor, with only large biases occurring in the Indonesian islands and along the coast of South America.

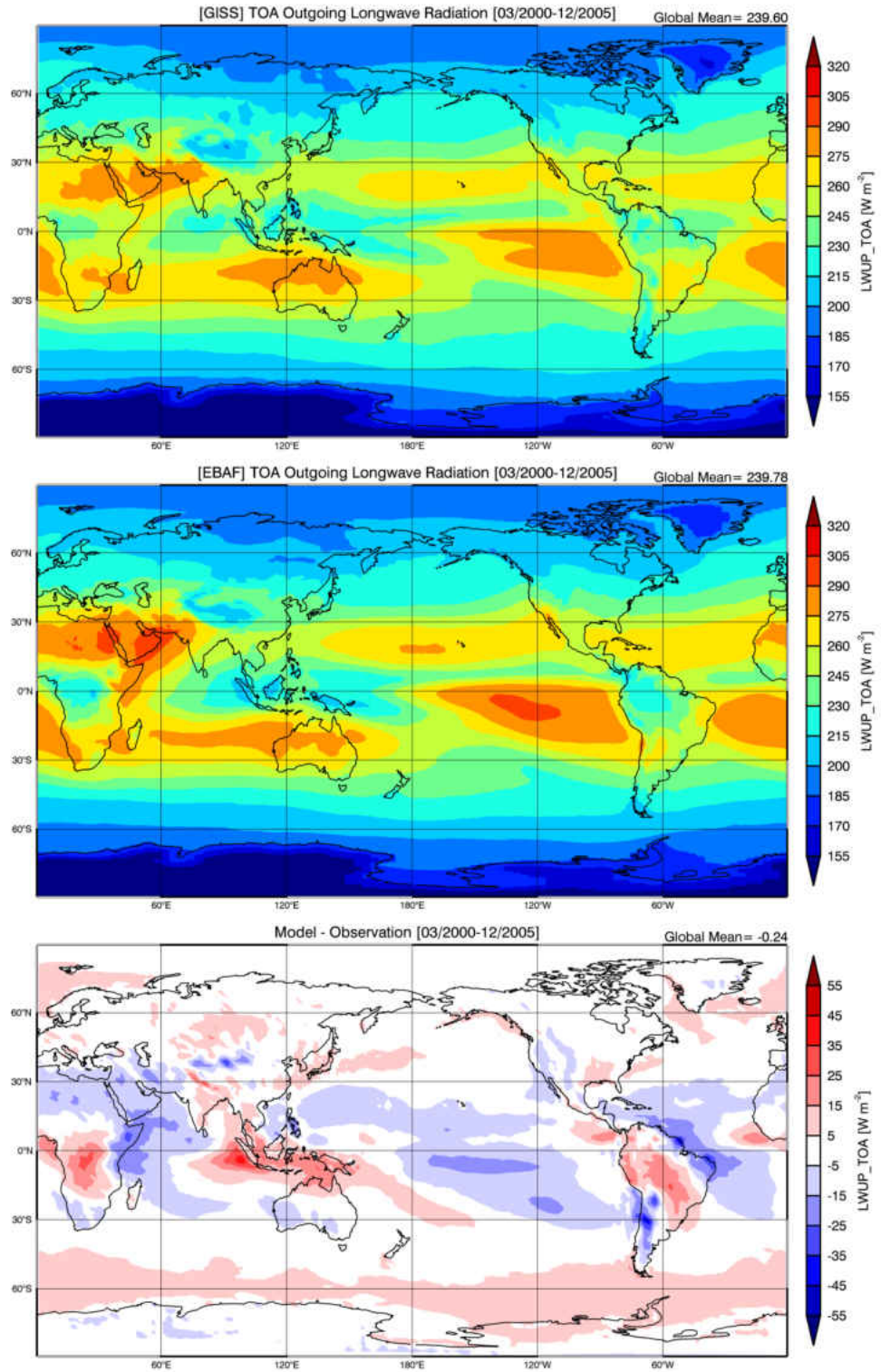


Figure 14. Outgoing longwave radiation (OLR) at TOA for the (a)GISS GCM, (b)EBAF observations, and the difference (c)GISS – EBAF, for the period of March 2000 through December 2005.



Modeled and observed OLRs show a high correlation over the SML, with only a  $3 \text{ W m}^{-2}$  difference between the two ( $231 \text{ W m}^{-2}$  and  $228 \text{ W m}^{-2}$ , respectively). This small bias is what we expect since a high percentage of the clouds over the SML are low-level clouds, below 680 mb, and their cloud-top temperatures are close to sea surface temperatures (Stubenrauch, 2010).

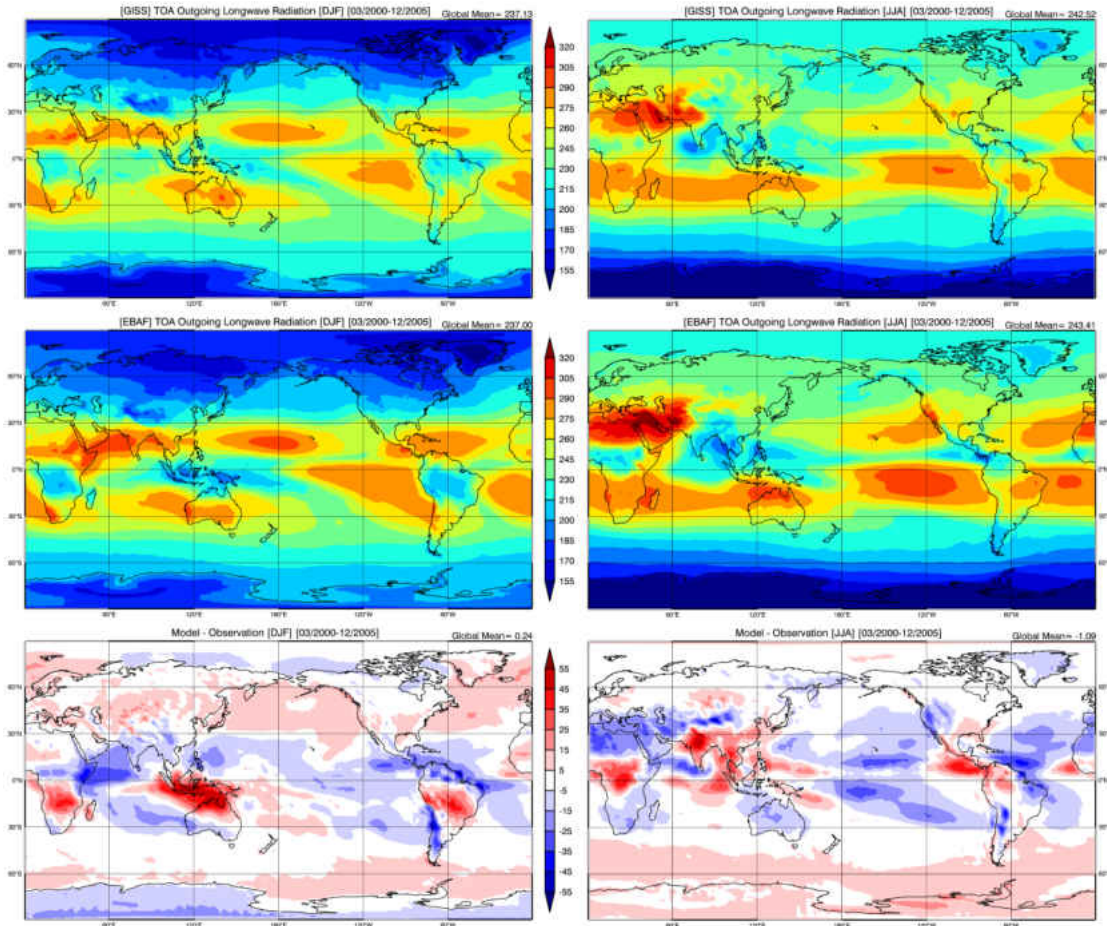


Figure 15. Same as Figure 14, except split seasonally into northern hemispheric winter (DJF, left) and summer (JJA, right).

Seasonal OLR biases, Figure 15c, show increased small-scale variability than with previous comparisons. Close examination of the model simulations and observations shows that the GCM simulates the basic pattern seen in observations, but fails to capture the full magnitude of seasonal variations. More specifically, the model

oversimulates in regions of low observed OLR and undersimulates in regions of high observed OLR. Regions with the highest biases, shown in Figure 15c, are mostly confined to the tropical regions, with only minor biases shown in the mid-latitude and polar regions. Regional biases appear to balance, resulting in modeled global means in perfect agreement with observations during both DJF and JJA seasons.

Over the SML, seasonal biases are mostly small, +1 and +5  $\text{W m}^{-2}$  during summer and winter, respectively, with the largest biases occurring over land and outside of the focus region in the southern tip of South America. Like the annual comparison shown previously, this small bias over the SML is expected because of the undersimulation of low-level clouds by the model, which have similar cloud-top temperatures to sea-surface temperatures.

#### *Net Flux*

Combining SW and LW flux using the following method (3), net flux at TOA for model simulations and observations are calculated and presented in Figure 16.

$$Net = ( SW \downarrow - SW \uparrow - OLR ) \quad (3)$$

Latitudinally-weighted global averages show that the modeled net flux at TOA agrees with observations within 1  $\text{W m}^{-2}$  (2 and 1  $\text{W m}^{-2}$ , respectively). Global comparisons show that the model undersimulates TOA net flux across the ITCZ and within the tropical boundaries. Because of the difficulty simulating marine stratocumulus clouds in the GCM, the model undersimulates the amount of reflected shortwave over these regions, leading to an oversimulation in net flux across these regions. Similarly, the model undersimulates the amount of low-level clouds in the SML, causing the modeled

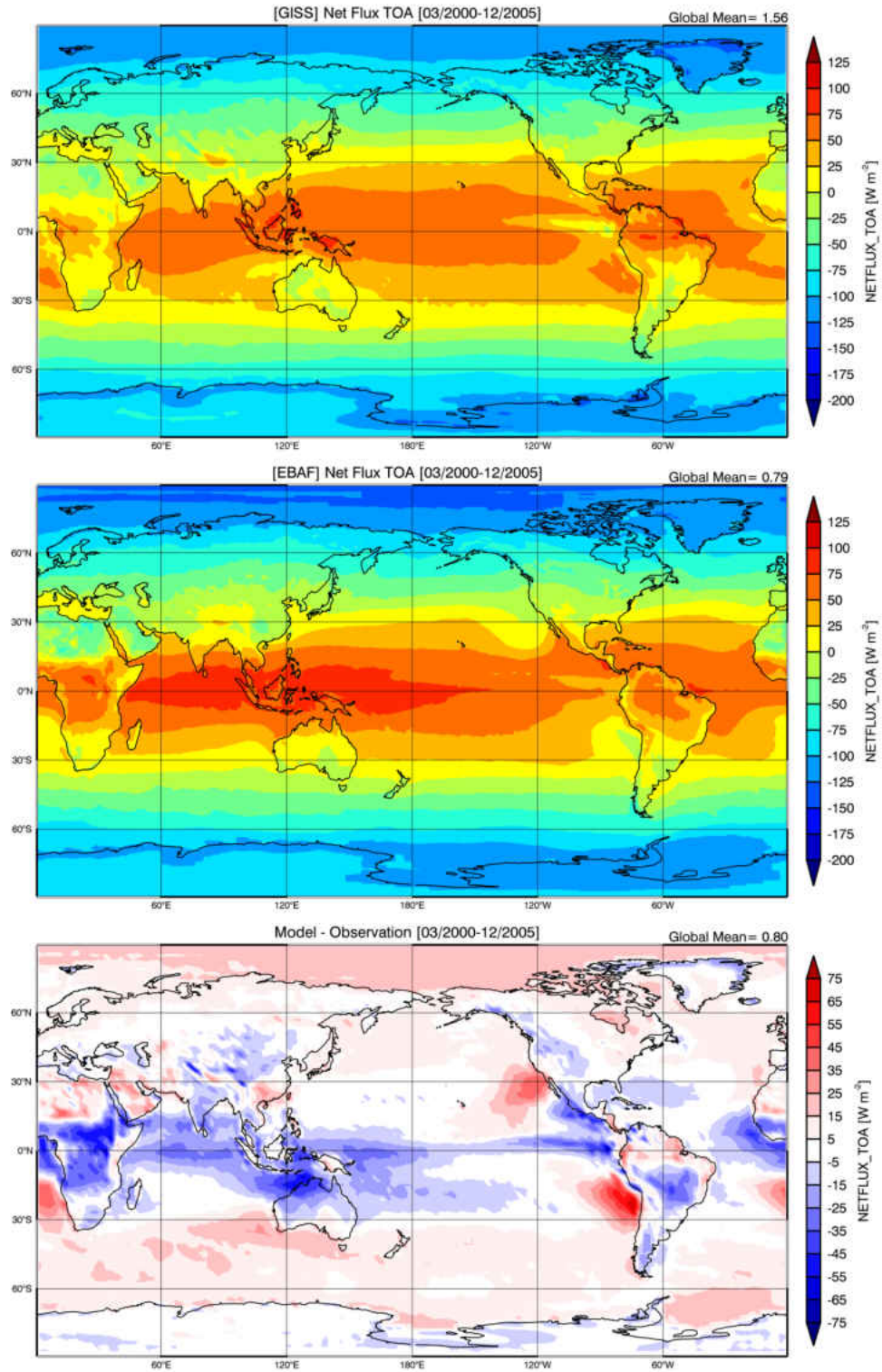


Figure 16. Net flux at TOA for the (a)GISS GCM, (b)EBAF observations, and the difference (c)GISS – EBAF, for the period of March 2000 through December 2005.



TOA net flux to be  $10 \text{ W m}^{-2}$  higher than observations across the SML (-14 and  $-24 \text{ W m}^{-2}$ , respectively).

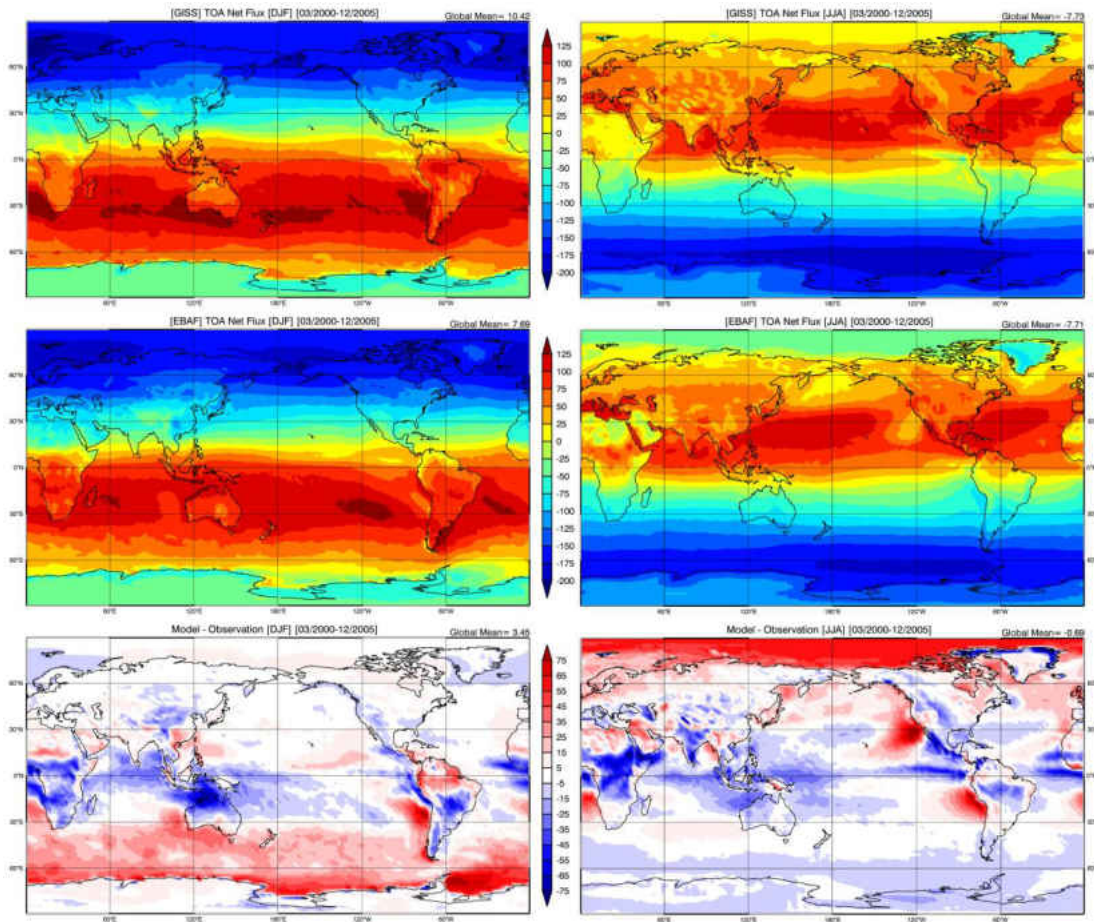


Figure 17. Same as Figure 16, except split seasonally into northern hemispheric winter (DJF, left) and summer (JJA, right).

Figure 17 shows the seasonal comparison in TOA net flux. Similar to the annual comparison, modeled TOA net fluxes are lower than observations across the ITCZ and tropical regions for each season. Net fluxes within marine stratocumulus regions are greatly oversimulated during each respective hemisphere summer, due to the increase in incident solar radiation combined with undersimulations of cloud fraction and albedo. Simulated global mean net flux is in close agreement with observations, with a positive bias of only  $2 \text{ W m}^{-2}$  during DJF and zero bias during JJA.

Across the SML, modeled TOA net flux is much higher than observations during southern hemisphere summer (104 and 82  $\text{W m}^{-2}$ , respectively), due to the undersimulation of low-level clouds. During the southern hemisphere winter however, the difference is much less than its summer counterpart, with a small negative bias of 1  $\text{W m}^{-2}$  across the SML (-126 and -127  $\text{W m}^{-2}$ ).

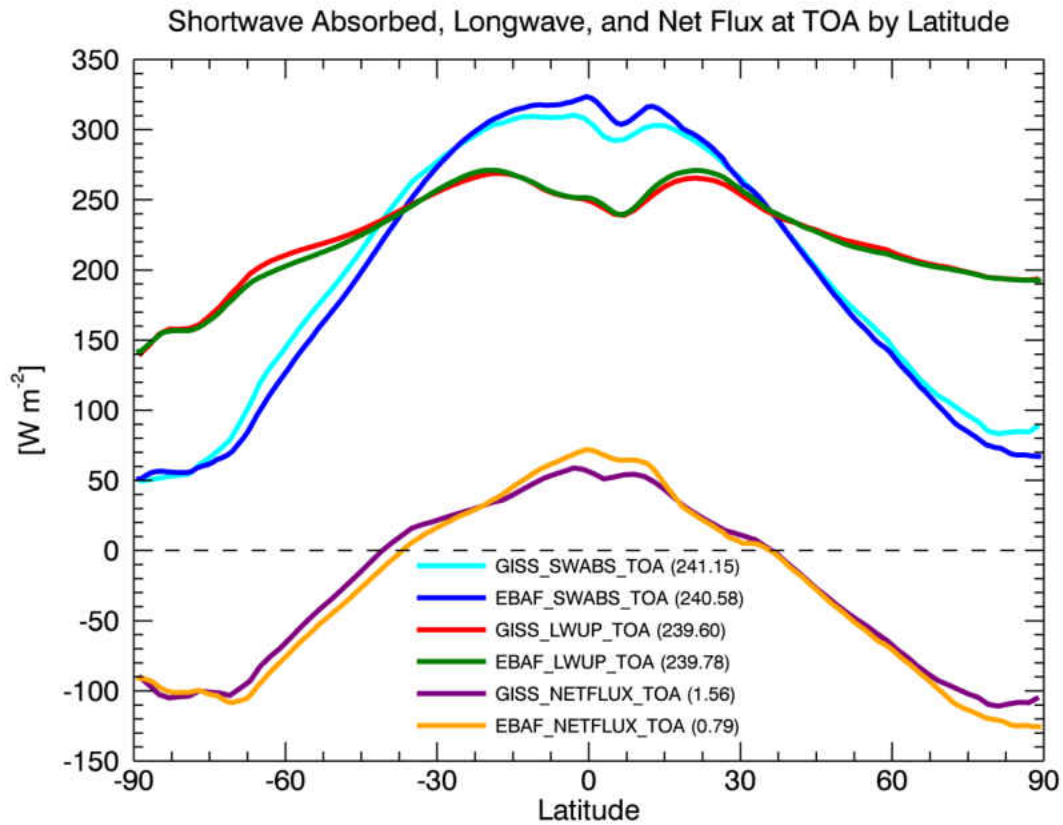


Figure 18. Absorbed shortwave radiation, outgoing longwave radiation, and net flux for the GISS GCM and CERES EBAF results, averaged by latitude, over the period of March 2000 through December 2005.

Figure 18 shows average shortwave absorption, outgoing longwave, and net fluxes across each latitudinal band, illustrating the latitudinal imbalance in radiation fluxes across the Earth. For example, in tropical regions, 30°S to 30°N, more SW energy is absorbed by the Earth-atmosphere system than emitted OLR, leaving a surplus of



energy over this region. This surplus energy is then transmitted pole-ward into the polar regions, where there exists a deficit of energy, through atmospheric and oceanic circulations (Hartmann, 1994).

Figure 18 also summarizes the results from Figures 12-20, and outlines where the largest biases occur. For example, two regions stand out in these results; the ITCZ/tropics, and the SML. In the ITCZ, a strong negative bias is shown in the model due to the increased population of clouds along the ITCZ from the previously discussed double ITCZ issue. Within the SML, a large positive bias in absorbed SW flux occurs due to undersimulation of low-level clouds over that region.

### PART 3: Cloud Radiative Effects (CRE)

CRE, the change in the net radiation budget due to clouds [Ramanathan et al., 1989; Dong and Mace, 2003; Dong et al., 2006], represents the bulk effect of clouds on the net radiation budget. It is a simple but effective means of studying cloud-radiation interactions and diagnosing problems in GCMs. The CRE is the difference between the net fluxes (down minus up) for all-sky conditions of SW and LW and for respective clear-sky conditions, in which  $CF = 0$ , defined as

$$\begin{aligned} CRE_{SW}(TOA) &= (SW_{all}^{\downarrow} - SW_{all}^{\uparrow}) - (SW_{clear}^{\downarrow} - SW_{clear}^{\uparrow}) \\ &= SW_{clear}^{\uparrow} - SW_{all}^{\uparrow} \end{aligned} \quad (4a)$$

and

$$\begin{aligned} CRE_{LW}(TOA) &= (LW_{all}^{\downarrow} - LW_{all}^{\uparrow}) - (LW_{clear}^{\downarrow} - LW_{clear}^{\uparrow}) \\ &= LW_{clear}^{\uparrow} - LW_{all}^{\uparrow} \end{aligned} \quad (4b)$$

respectively. The NET CRE,  $CRE_{NET}$ , is the sum of  $CRE_{SW}$  and  $CRE_{LW}$  at TOA. Positive values of CRE indicate increased radiative flux at TOA due to the presence of clouds, and negative values denote a radiative energy loss. Positive and negative CREs lead to warming and cooling tendencies, respectively.

#### *Shortwave CRE ( $CRE_{SW}$ )*

To quantitatively estimate the impact of clouds on the TOA radiation budget, clear-sky fluxes must be explored first. Therefore, modeled reflected SW flux for clear-sky conditions and EBAF-TOA data from clear-sky CERES-MODIS retrievals are presented in Figure 19.

Except for the polar regions, the GCM appears to capture clear-sky reflected SW fairly well over oceanic regions. Oceanic results within the polar regions however may be questionable, due to the passive sensor aboard MODIS having trouble distinguishing cloud layers from highly reflective snow/ice surfaces, particular during polar night (Giannecchini et al. 2013). Over land, the model has scattered positive and negative biases that are fairly minor and localized. Overall, the model closely captures clear-sky reflected SW flux, simulating a global mean  $54 \text{ W m}^{-2}$  while observations measure  $52 \text{ W m}^{-2}$ , giving an oversimulation of  $2 \text{ W m}^{-2}$ .

Since the model appears to have fairly high accuracy over oceans, it is no surprise that GISS simulations are close to observations ( $42$  and  $38 \text{ W m}^{-2}$ , respectively), with a positive bias of  $4 \text{ W m}^{-2}$  over the SML. The same positive bias appears over the oceanic northern mid-latitudes as well, suggesting that this may be an issue in the model over the mid-latitudes.

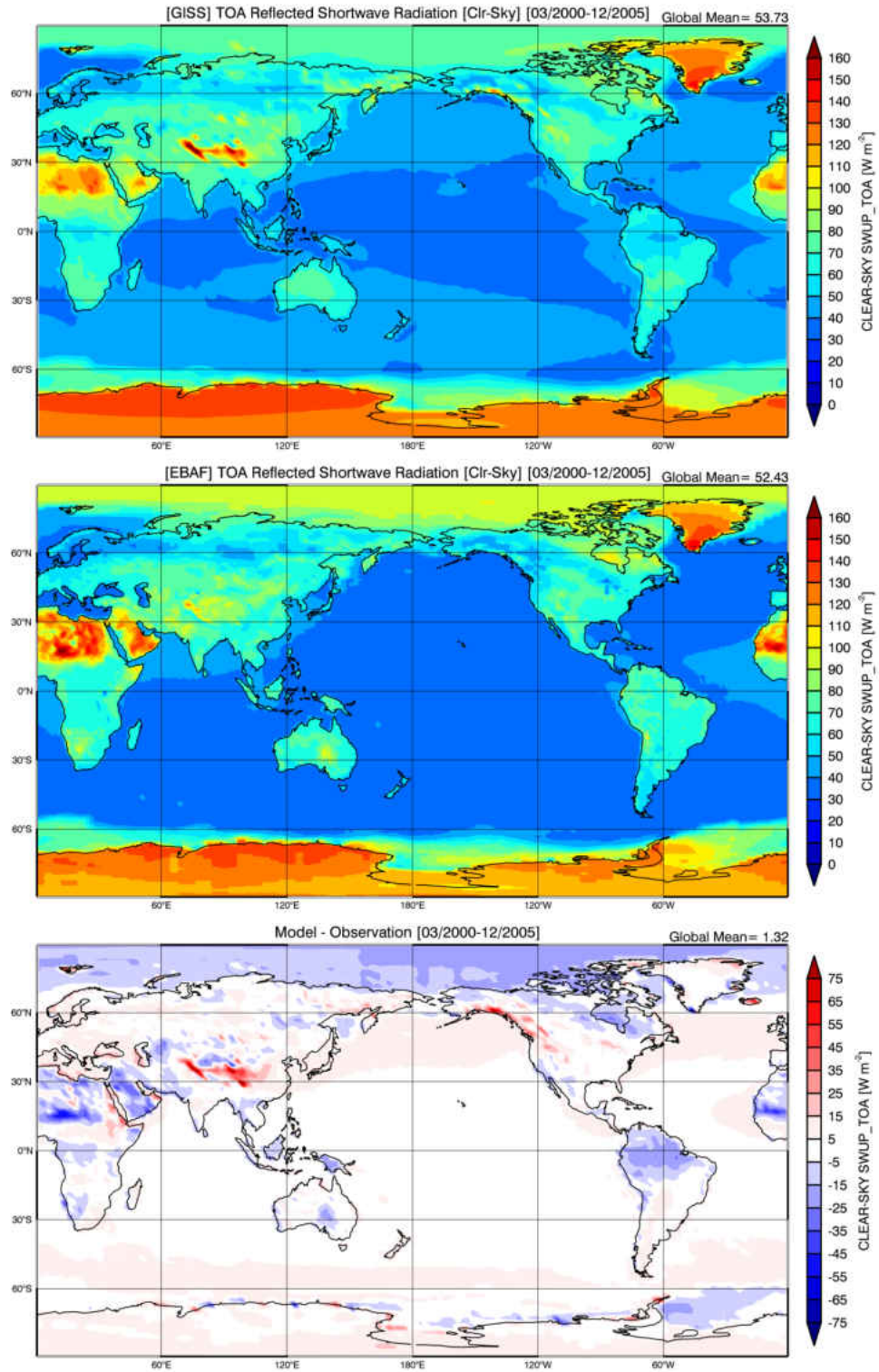


Figure 19. Reflected SW fluxes at TOA under clear-sky conditions for the (a)GISS GCM, (b)EBAF observations, and the difference (c)GISS – EBAF, for the period of March 2000 through December 2005.

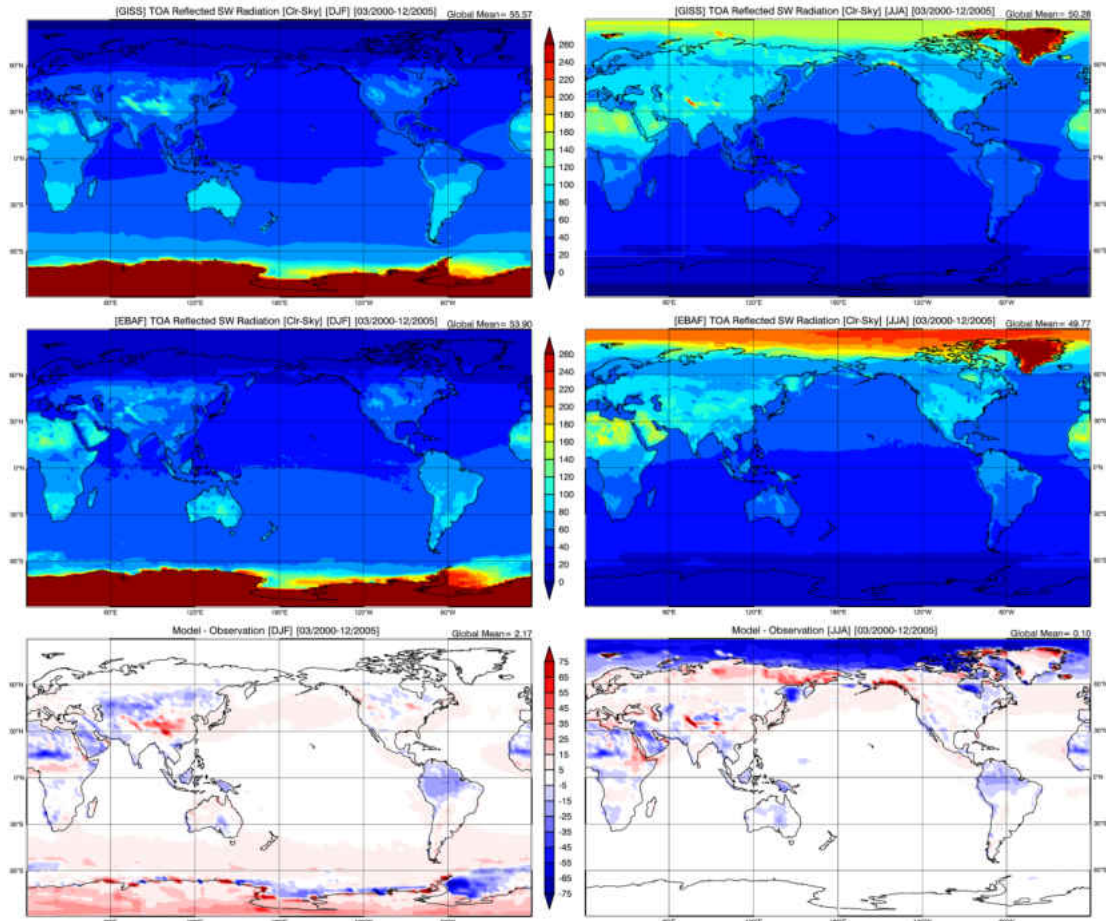


Figure 20. Same as Figure 19, except split seasonally into northern hemispheric winter (DJF, left) and summer (JJA, right).

Seasonal biases, shown in Figure 20, stay consistent over oceans but increase poleward during each summer, with a positive bias over Antarctic regions during DJF and a negative bias over Arctic regions during JJA. Biases over land are slightly larger than those over the ocean, and are largely consistent in sign seasonally, with a few minor shifts occurring in the northern mid-latitudes and western Australia. Global mean biases are minimal during both DJF and JJA, with a model bias of  $+2 \text{ W m}^{-2}$  during DJF and no bias during JJA.

With most of the seasonal and annual biases occurring over land features, the SML simulations closely resemble seasonal observations. A positive model bias of  $7 \text{ W}$

$\text{m}^{-2}$  appears during southern hemisphere summer (55 and 48  $\text{W m}^{-2}$ ), which is then reduced when combined with other seasons to create annual data, such as the positive model bias found during winter of 2  $\text{W m}^{-2}$  (28 and 26  $\text{W m}^{-2}$ ).

Using the clear-sky results shown above and all-sky results shown previously in part 2,  $\text{CRE}_{\text{SW}}$  is calculated using Equation 4a and presented in Figure 21, where positive values of CRE indicate warming and negative CRE values denote cooling of the earth-atmospheric system. In general, clouds have a higher albedo than clear skies resulting in negative CREs, such as deep convective clouds over the ITCZ and marine stratocumulus clouds over the NML and SML regions. However, there are a few regions where clear-sky albedos are higher than cloud albedos, such as polar and desert regions, resulting in positive CREs as demonstrated in Figure 21.

As discussed in Part II, the reflected SW flux has a strong positive correlation with CF, which results in a strong negative correlation between  $\text{CRE}_{\text{SW}}$  and CF. Therefore, higher CFs will create a greater cooling effect. Of particular interest is the strong negative relationship between CF comparison in Figure 2c and  $\text{CRE}_{\text{SW}}$  comparison in Figure 21c. It is noticed that the negative  $\text{CRE}_{\text{SW}}$  biases in Figure 23c correspond very well with the positive CF biases over the ITCZ, and vice versa over the NML and SML regions. Because modeled and observed clear-sky fluxes are in excellent agreement, the biases in  $\text{CRE}_{\text{SW}}$  are mainly resulting from CF and reflected SW flux differences between the model and observations. More clouds generate a higher reflected SW flux and strong negative  $\text{CRE}_{\text{SW}}$ , and eventually result in a strong cooling effect on the Earth-atmospheric system.



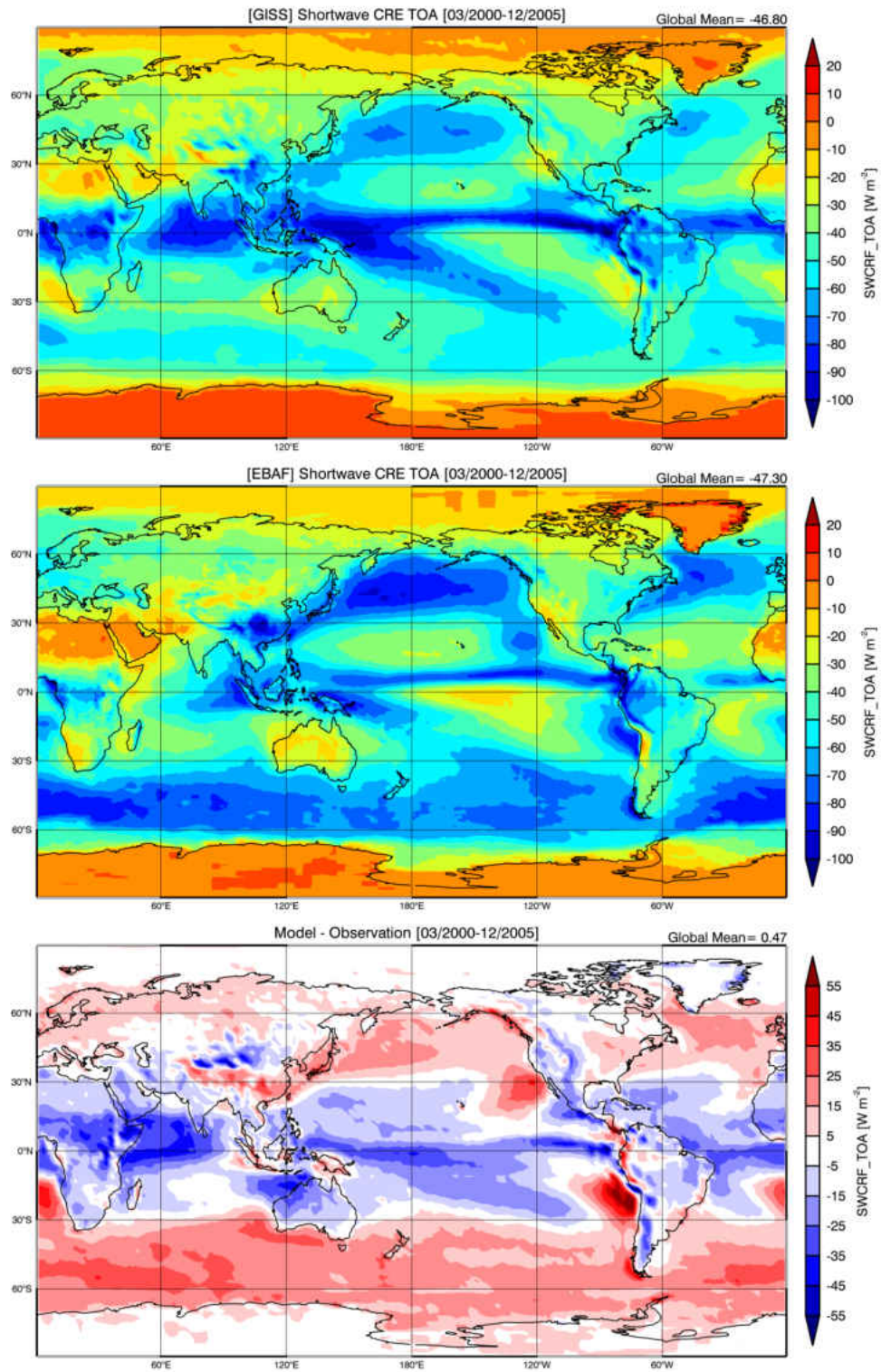


Figure 21. SW CRE at TOA for the (a)GISS GCM, (b)EBAF observations, and the difference (c)GISS – EBAF, for the period of March 2000 through December 2005.

Over the SML, modeled  $CRE_{SW}$  is  $-50 \text{ W m}^{-2}$  while a  $CRE_{SW}$  of  $-67 \text{ W m}^{-2}$  is observed, resulting in a drastic undersimulation of  $17 \text{ W m}^{-2}$  in  $CRE_{SW}$ . This undersimulation is specifically due to the lack of low-level clouds being produced by the GCM over the SML, resulting in less reflected SW flux in the model.

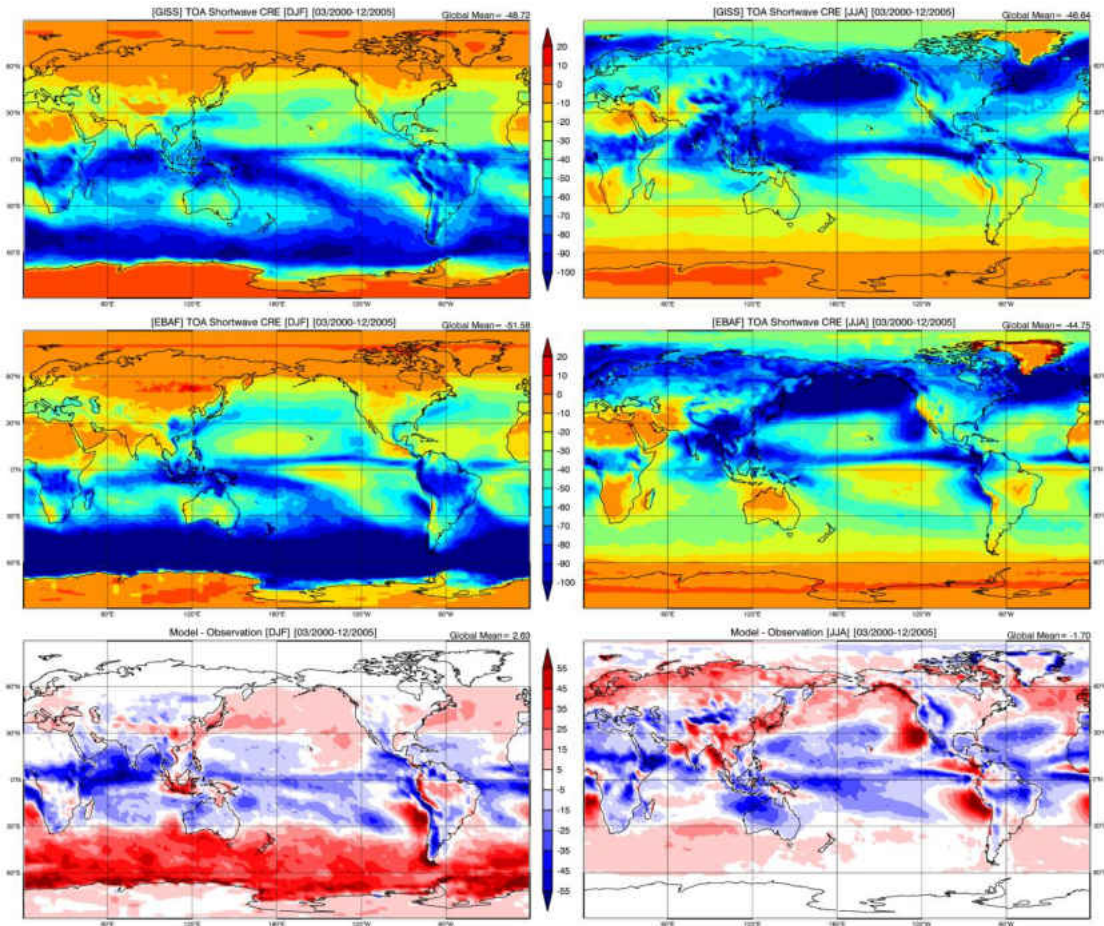


Figure 22. Same as Figure 21, except split seasonally into northern hemispheric winter (DJF, left) and summer (JJA, right).

Seasonal comparisons in  $CRE_{SW}$ , shown in Figure 22, show the same patterns as the  $CRE_{SW}$  annual comparison in Figure 21. For example, a strong positive bias in  $CRE_{SW}$  over the SML during DJF strongly correlates with a negative bias in CF, and a negative bias in  $CRE_{SW}$  over the ITCZ strongly correlates with a positive bias in CF. Modeled global mean  $CRE_{SW}$  is in close agreement with observations, with an

oversimulation of  $3 \text{ W m}^{-2}$  during DJF ( $-49$  and  $-52 \text{ W m}^{-2}$ , respectfully), and an undersimulation of  $2 \text{ W m}^{-2}$  during JJA ( $-47$  and  $-45 \text{ W m}^{-2}$ , respectfully). The strongest biases in  $\text{CRE}_{\text{SW}}$  over the SML occur during summer ( $-80$  and  $-106 \text{ W m}^{-2}$ ), when a higher zenith angle results in increased incident solar radiation. The model more closely simulates  $\text{CRE}_{\text{SW}}$  during the winter, when the model undersimulates  $6 \text{ W m}^{-2}$  of cooling ( $-23$  and  $-29 \text{ W m}^{-2}$ ).

#### *Longwave CRE ( $\text{CRE}_{\text{LW}}$ )*

To investigate the impact of clouds on the TOA LW radiation budget, clear-sky OLR and  $\text{CRE}_{\text{LW}}$  will be explored and compared with observations. Clear-sky OLR results, shown in Figure 23, must first be explored before comparing  $\text{CRE}_{\text{LW}}$ .

The GCM simulates a global clear-sky OLR pattern that is similar to the pattern seen in observations, as shown in Figure 23. However, their difference (Figure 23c) shows a nearly constant negative bias of about  $-10 \text{ W m}^{-2}$  from  $60^\circ\text{S}$  to  $60^\circ\text{N}$ , and even more in some regions, with a globally averaged difference of  $-8 \text{ W m}^{-2}$ . This gross undersimulation of clear-sky OLR by the model is due to the dry bias that exists when comparing model output with observational datasets. To obtain clear-sky samples from observations, clear-sky scenes are first identified by the CERES cloud retrieval algorithms, and then clear-sky fluxes observed by the CERES sensors on Terra and Aqua are collected and averaged into the CERES EBAF dataset.

In this study, CRE is determined by the difference between the net surface fluxes with and without the presence of clouds. As discussed in Dong et al. (2006), CRE should be the difference between the net fluxes under cloudy and clear-sky conditions during cloudy periods. Since it is impossible to measure clear-sky fluxes under cloudy



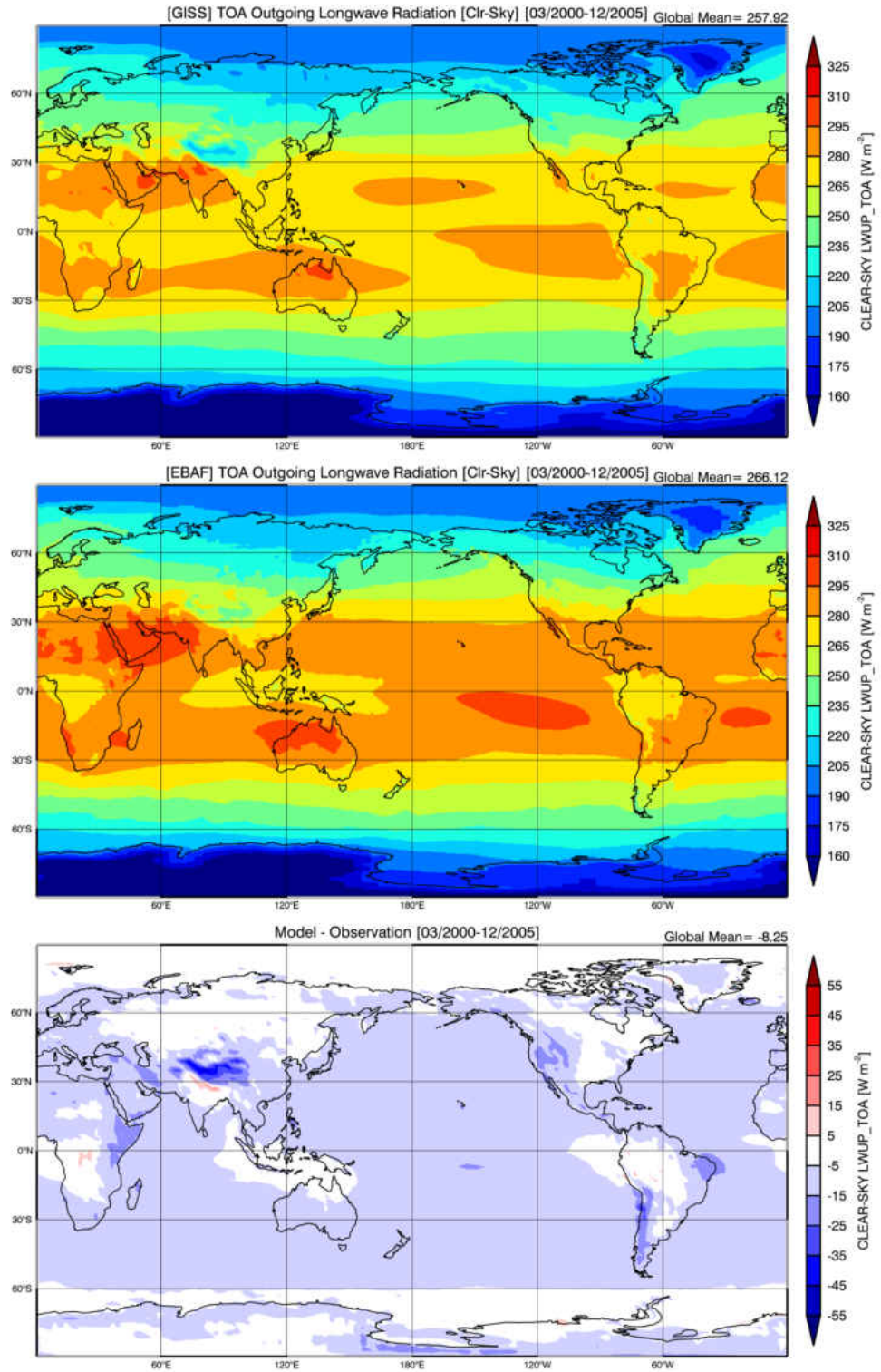


Figure 23. OLR at TOA under clear-sky conditions for the (a)GISS GCM, (b)EBAF observations, and the difference (c)GISS – EBAF, for the period of March 2000 through December 2005.

conditions, the determination of clear-sky values is another potential source of uncertainty in calculating CRE from observational data. As demonstrated in Figure 10 of Dong et al. (2006), the atmospheric perceptible water vapor (PWV) amounts during cloudy conditions are much higher than those during clear-sky conditions, which may result in higher clear-sky OLRs calculated from satellite retrievals than those under actual conditions for calculating CRE.

Clear-sky samples in the GCMs, however, are created by taking a scene and removing the cloud contamination within the scene. While the clouds are technically removed, the dynamic and thermodynamic conditions that made it favorable to form a cloud are still present, including upper tropospheric water vapor in the atmosphere (Sohn et al. 2006). This leads to a dry bias, where clear-sky samples in GCMs contain much more water vapor in the upper troposphere of the atmosphere compared to observations, resulting in a decrease in GCM simulated OLR. This dry bias was shown in Sohn et al. (2006) to contribute up to  $12 \text{ W m}^{-2}$  by trapping OLR. Directly comparing PWVs simulated by the GISS GCM and observed by A-train satellites, further confirms the findings of the Sohn et al. (2006) study, where modeled PWVs agree very well with observations at all levels, but are much higher around 100 mb (Jiang et al. 2012, Su et al. 2012).

In the SML, the observed and simulated clear-sky OLRs of  $258$  and  $249 \text{ W m}^{-2}$ , respectively, give a dry bias of  $11 \text{ W m}^{-2}$ , which is close to the globally weighted mean dry bias of  $8 \text{ W m}^{-2}$ . Sohn et al. (2008) found that the redistribution of water vapor associated with convection results in a significant contribution to CRF through the upper tropospheric moistening in the tropics, whereas columnar water vapor variation

dominates OLR over the mid-latitudes. Results shown here are larger than results found in Sohn et al. (2008), and can only be explained by the gross oversimulation of columnar water vapor by the GCM over the SML.

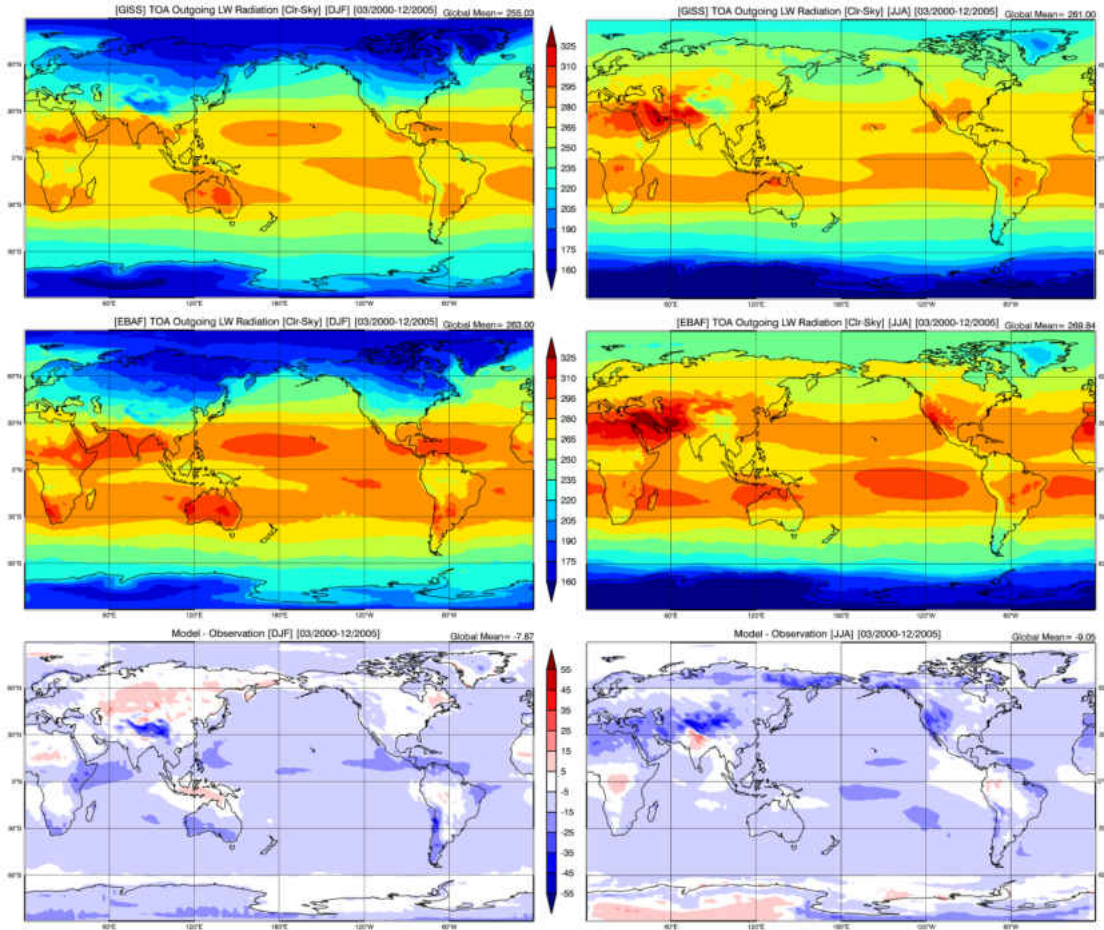


Figure 24. Same as Figure 23, except split seasonally into northern hemispheric winter (DJF, left) and summer (JJA, right).

Seasonal results, shown in Figure 24, show that strong negative biases are maintained year-round across Tibet, China. Red areas in Figure 24c represent the regions where clear-sky OLR is oversimulated enough to actually overcome the dry bias. Across the SML, there is a consistent negative dry bias across all seasons, which plays a large role in assessing  $CRE_{LW}$ , and thus the  $CRE_{NET}$  effect as well. Both globally and over the SML, the dry bias stays consistent at around 8 to 10  $W m^{-2}$ .

The following  $CRE_{LW}$  results were calculated using the same method as calculating  $CRE_{SW}$  (Equation 4b). Because  $CRE_{LW}$  at TOA is calculated as clear-sky OLR minus all-sky OLR, Figure 25 shows how much energy is trapped due to the presence of clouds.

CRE is directly related to clouds and their impact on the radiation budget, and so results should correlate well with cloud fraction results shown in Figure 2. The GCM simulates a weighted global mean  $CRE_{LW}$  of  $18 \text{ W m}^{-2}$  of heating, while observations measure  $26 \text{ W m}^{-2}$ , resulting in an underestimation of  $8 \text{ W m}^{-2}$ . Because all-sky simulations closely resembled observations, the negative bias in  $CRE_{LW}$  is derived predominately from the dry bias in clear-sky OLR.

Since the model undersimulates low-level clouds across the SML,  $CRE_{LW}$  biases within the SML tend to be higher than the global mean bias. Over the SML, the GCM simulates a  $CRE_{LW}$  of  $18 \text{ W m}^{-2}$ , while observations show  $31 \text{ W m}^{-2}$ , giving a total undersimulation in  $CRE_{LW}$  of  $13 \text{ W m}^{-2}$ , more than  $5 \text{ W m}^{-2}$  greater than the global mean bias. This gross undersimulation in LW radiative heating across the SML plays an important role in balancing out the SW cooling effect shown previously when calculating  $CRE_{NET}$ .



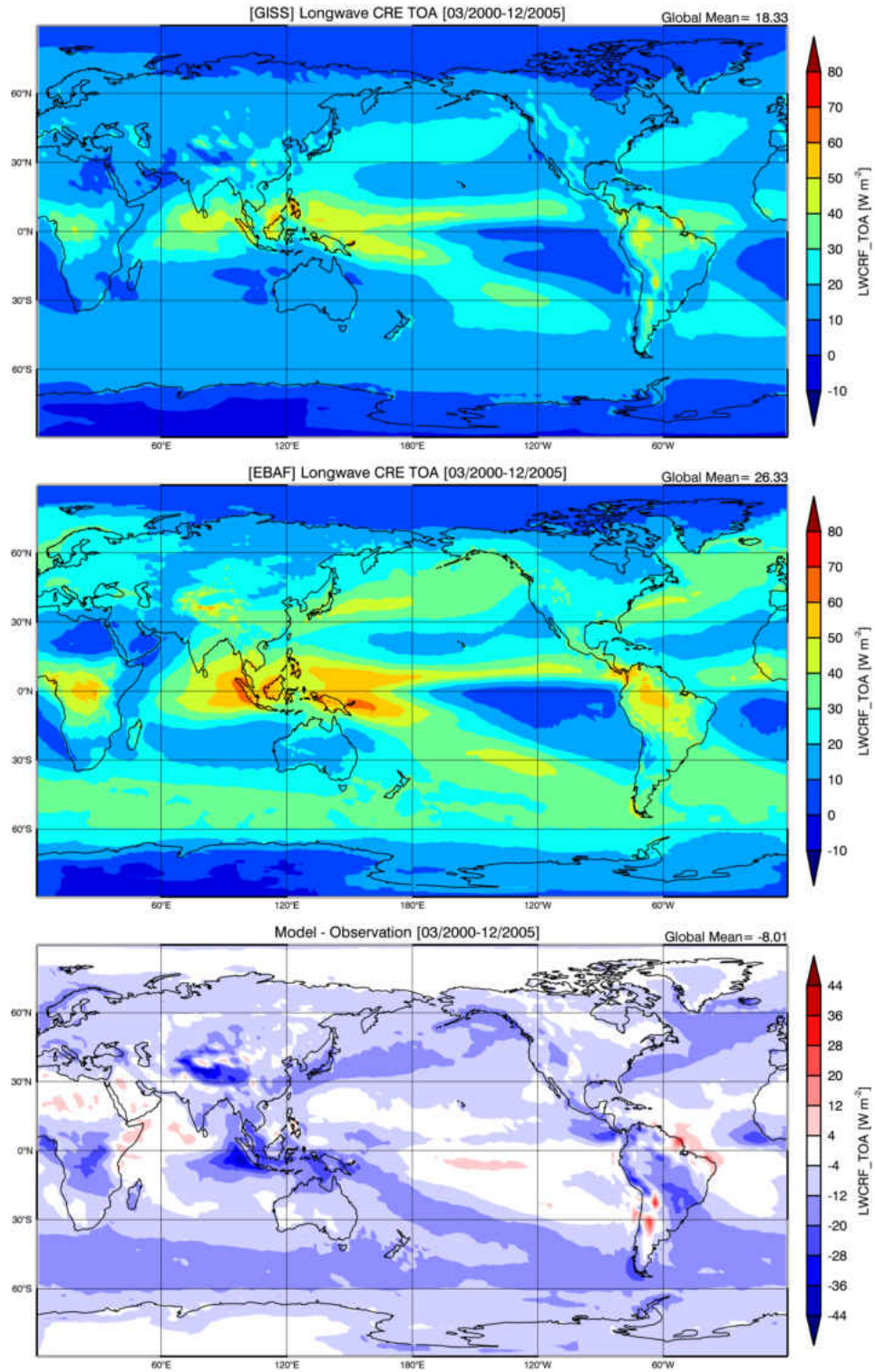


Figure 25. LW CRE at TOA for the (a)GISS GCM, (b)EBAF observations, and the difference (c)GISS – EBAF, for the period of March 2000 through December 2005.

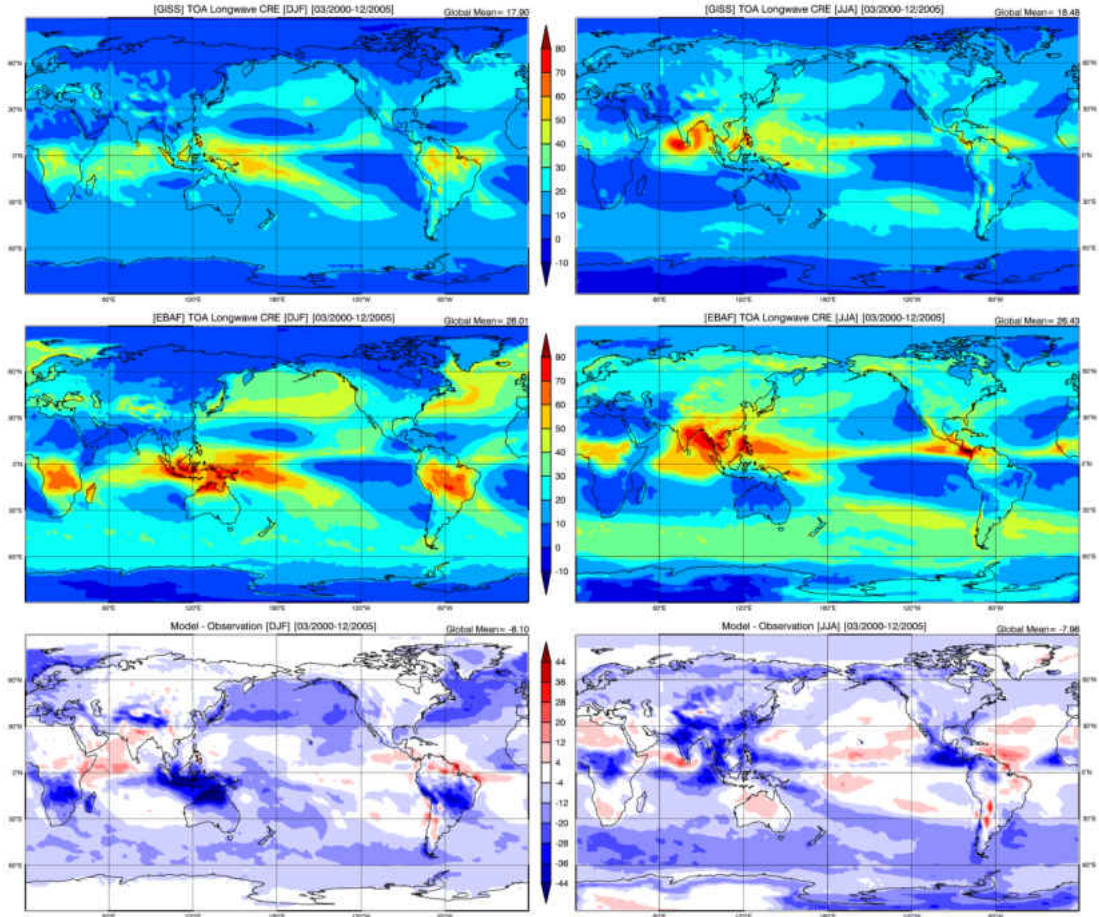


Figure 26. Same as Figure 25, except split seasonally into northern hemisphere winter (DJF, left) and summer (JJA, right).

An interesting pattern occurs when looking at the seasonal results shown in Figure 26c. Biases within the tropics increase/decrease with decreased/increased solar zenith angle, while biases within the mid-latitudes and polar regions increase/decrease with increased/decreased solar zenith angle. This pattern is present in the all-sky OLR biases shown in Figure 15c, and because clear-sky OLR biases are fairly constant globally, these patterns emerge in  $CRE_{LW}$  results as well. It is hypothesized that these biases are due to the model undersimulation of the seasonal variation in OLR.

The largest seasonal bias of  $CRE_{LW}$ ,  $-14 \text{ W m}^{-2}$ , occurs across the SML during southern hemisphere winter ( $19$  and  $33 \text{ W m}^{-2}$ ), when solar zenith angle is higher and the

model shows a higher oversimulation of all-sky OLR, compared to a negative bias of  $-10 \text{ W m}^{-2}$  during summer ( $17$  and  $27 \text{ W m}^{-2}$ ).

#### *Net CRE ( $CRE_{NET}$ )*

The  $CRE_{NET}$  is simply the sum of SW and LW CREs, as used in Ramanathan et al. (1989) and Cess et al. (1997), and represents the net effect of clouds on TOA radiation budget. Annual results of net CRE for the GISS GCM, CERES-MODIS observations, and the difference between the two are presented in Figure 27.

The modeled and observed global averaged NET CREs of  $-28 \text{ W m}^{-2}$  and  $-21 \text{ W m}^{-2}$ , respectively, give a global weighted mean bias of  $7 \text{ W m}^{-2}$  of atmospheric cooling oversimulated by the GCM. Considering the GCM undersimulates clear-sky OLR globally by over  $8 \text{ W m}^{-2}$  due to the global dry bias, an oversimulation of  $8 \text{ W m}^{-2}$  suggests a high degree of accuracy by the GCM in simulating  $CRE_{NET}$ . Directly comparing Figure 27c with Figure 2c illustrates that regions with positive/negative biases in  $CRE_{NET}$  have strong correlations with negative/positive biases in CF. Of more interest is the strong relationship between regional TOA  $CRE_{NET}$  biases and TOA  $CRE_{SW}$  biases in Figure 21c, and with TOA reflected SW biases in Figure 10c, except for polar regions. These comparisons suggest that TOA reflected SW biases directly influence TOA  $CRE_{SW}$  results, and therefore result in regional  $CRE_{NET}$  biases.



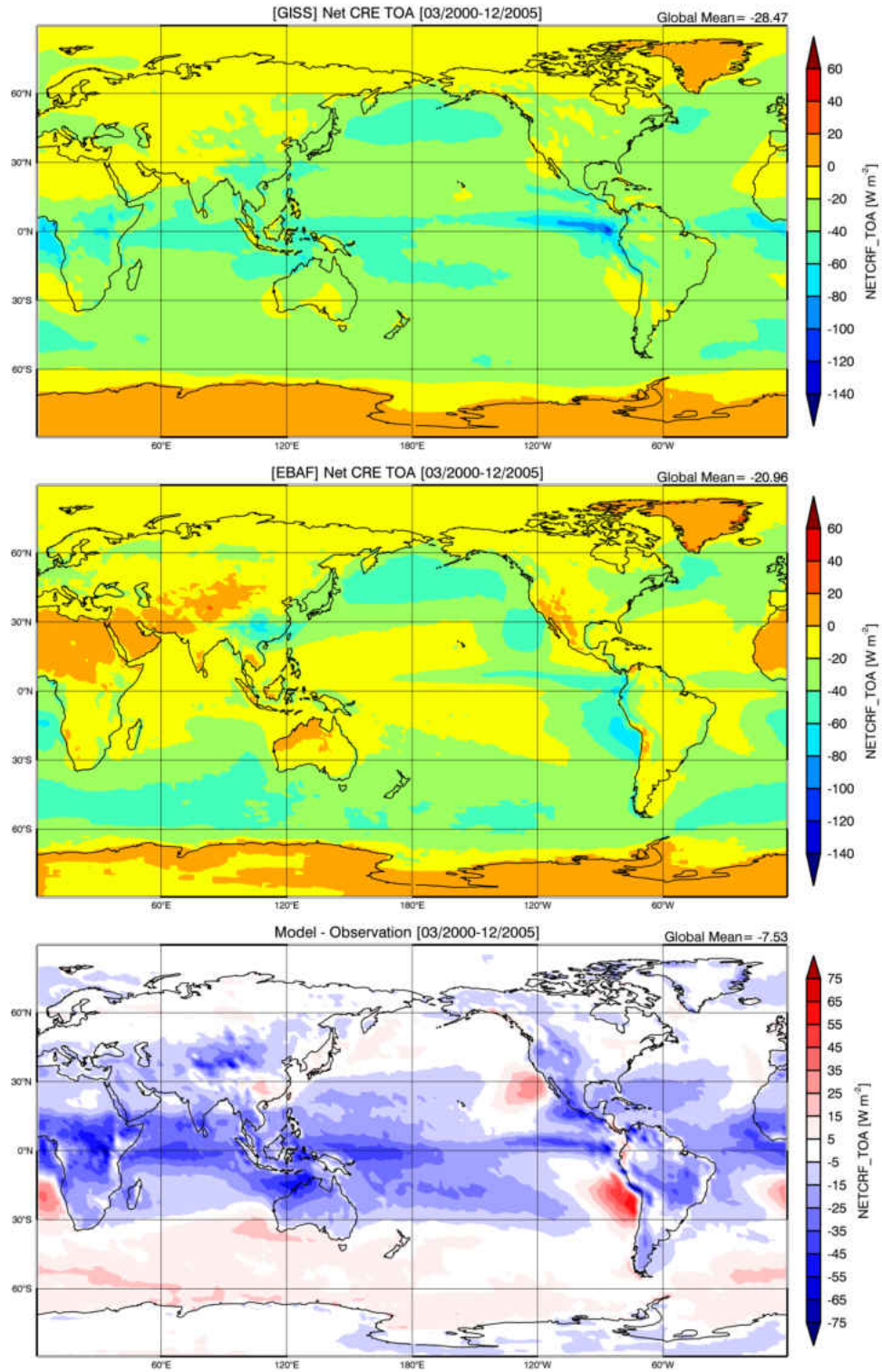


Figure 27. Net CRE at TOA for the (a)GISS GCM, (b)EBAF observations, and the difference (c)GISS – EBAF, for the period of March 2000 through December 2005.



This is seen over the SML where the GCM simulates a  $CRE_{NET}$  of  $-32 \text{ W m}^{-2}$  while observations measure  $-37 \text{ W m}^{-2}$ , leading to an undersimulation in atmospheric cooling of  $5 \text{ W m}^{-2}$ . Given the impact of the dry bias on  $CRE_{NET}$ , this shows that the model actually grossly undersimulates the amount of cooling that occurs due to the clouds over the SML. This is known to be a side effect of the undersimulation of low-level clouds over the SML, resulting in minimal changes to all-sky TOA OLR while having large impacts on TOA all-sky reflected shortwave.

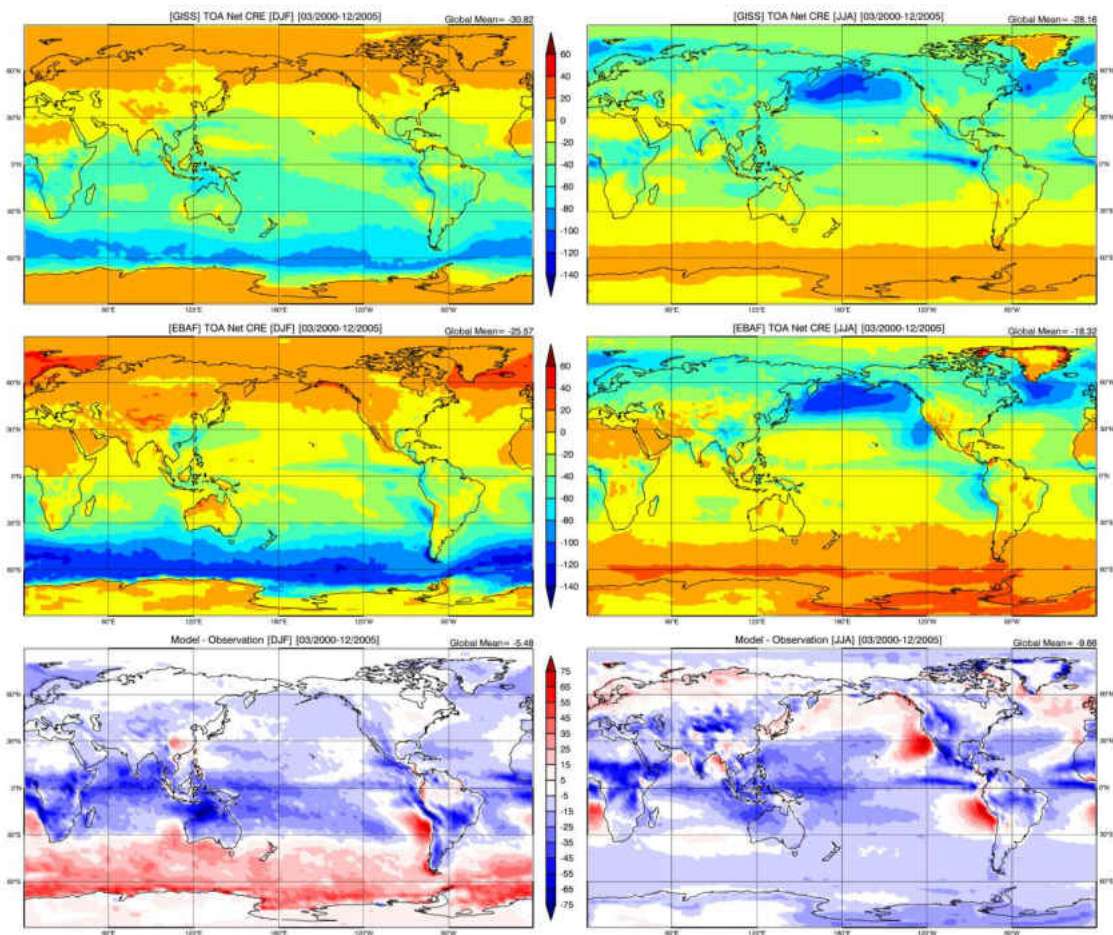


Figure 28. Same as Figure 27, except split seasonally into northern hemispheric winter (DJF, left) and summer (JJA, right).

Global seasonal biases show minimal change over the tropics each season, while model oversimulation of  $CRE_{NET}$  intensity increases over the mid-latitudes and within regions of marine stratocumulus as solar zenith angle decreases. Over the SML, the model strongly oversimulates TOA  $CRE_{NET}$  by  $17 \text{ W m}^{-2}$  during DJF ( $-62$  and  $-79 \text{ W m}^{-2}$ ), due to the drastic undersimulation in cloud fraction resulting in high TOA all-sky SW biases. During southern hemisphere winter when solar zenith angle is large, the model shows a slight undersimulation of  $8 \text{ W m}^{-2}$  in  $CRE_{NET}$  ( $-4$  and  $+4 \text{ W m}^{-2}$ ).

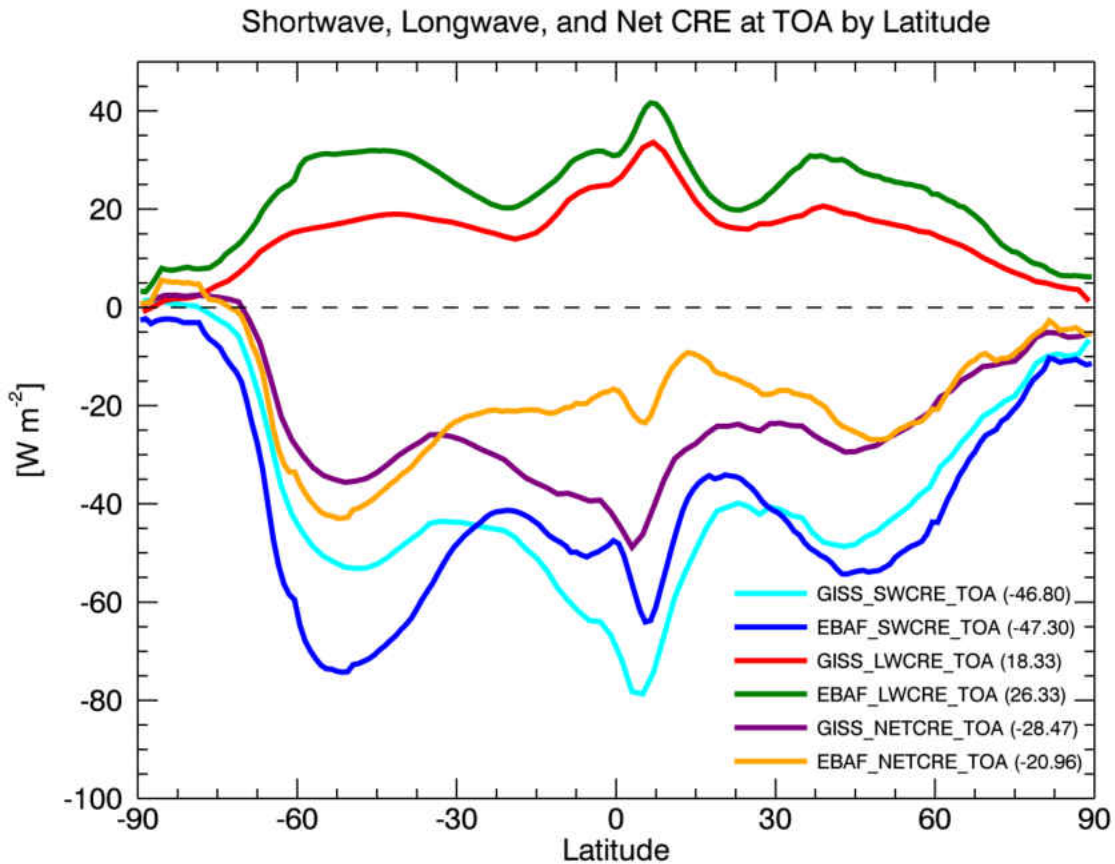


Figure 29. SW, LW, and NET CRE for the GISS GCM and CERES EBAF results, averaged by latitude, over the period of March 2000 through December 2005.

Figure 29 presents SW, LW, and NET CRE for the GISS model and CERES EBAF observations, averaged into latitudinal bands, which shows many prominent features discussed in this section: (1) The largest biases in  $CRE_{SW}$  are found over the

SML, where  $CRE_{SW}$  is drastically undersimulated by the model. With only minimal differences in clear-sky reflected SW, it is suggested that the primary contribution to undersimulation in  $CRE_{SW}$  is from the biases in all-sky reflected SW, which are due to the undersimulation of low-level clouds by the GISS model. (2)  $CRE_{LW}$  is undersimulated by the model globally. Minimal differences were found in all-sky OLR, meaning that most of the bias is derived from clear-sky OLR differences. This is known to be due to the dry bias in comparing GCMs with passive sensors. The dry bias is higher than expected however, and is hypothesized to be due to the gross oversimulation of modeled atmospheric water vapor at the 100-mb level. (3) The biases in SW and LW CRE cancel out to produce a fairly accurate simulation of  $CRE_{NET}$ .

CHAPTER V  
CONCLUSIONS

In this study, we assess clouds simulated by the NASA GISS-E2-R GCM and the impact of these clouds on the TOA radiation budget by comparing the model with observational results from CERES SYN1 and EBAF over the period of March 2000 through December 2005. Comparisons are conducted on a global scale and over the southern mid-latitudes (SML) to assess model performance both globally and regionally. A summary of the global averaged cloud properties, TOA radiation budgets, and CREs simulated from the GISS GCM and observed from CERES-MODIS, as well as their differences are shown in Table 4 and regionally over the SML in Table 5.

Table 4. Global (GBL) weighted means, standard deviations, and correlation for the GISS GCM and CERES-MODIS Observations.

Variable	Units	GISS GBL Avg	OBS GBL Avg	Comparison [GISS-OBS] GBL Avg	GISS GBL Std Dev	OBS GBL Std Dev	Comparison [GISS-OBS] GBL Std Dev	Corr
CF	[%]	61	62	-1	14	15	16	0.28
TWP	[ $g\ m^{-2}$ ]	188	118	70	113	74	101	0.43
SW $\uparrow$ TOA	[ $W\ m^{-2}$ ]	101	100	1	18	17	15	0.96
SW( $\downarrow\uparrow$ ) TOA	[ $W\ m^{-2}$ ]	241	241	0	91	96	15	0.99
LW $\uparrow$ TOA	[ $W\ m^{-2}$ ]	240	240	0	35	37	7	0.97
Net Flux TOA	[ $W\ m^{-2}$ ]	2	1	1	60	65	13	0.98
C_SW $\uparrow$ TOA	[ $W\ m^{-2}$ ]	54	52	2	29	30	9	0.97
SW CRE	[ $W\ m^{-2}$ ]	-47	-47	0	23	24	15	0.83
C_LW $\uparrow$ TOA	[ $W\ m^{-2}$ ]	258	266	-8	40	42	5	0.99
LW CRE	[ $W\ m^{-2}$ ]	18	26	-8	9	12	6	0.80
Net CRE	[ $W\ m^{-2}$ ]	-28	-21	-7	16	16	13	0.80

Table 5. Weighted means, standard deviations, and correlation across the southern mid-latitudes (SML) for the GISS GCM and CERES-MODIS Observations.

Variable	Units	GISS SML Avg	OBS SML Avg	Comparison [GISS-OBS] SML Avg	GISS SML Std Dev	OBS SML Std Dev	Comparison [GISS-OBS] SML Std Dev	Corr
CF	[%]	58	79	-21	10	7	6	0.65
TWP	[ $g\ m^{-2}$ ]	202	200	2	44	46	47	0.20
SW $\uparrow$ TOA	[ $W\ m^{-2}$ ]	92	105	-13	6	7	6	0.98
SW( $\downarrow\uparrow$ ) TOA	[ $W\ m^{-2}$ ]	217	202	15	43	44	6	0.99
LW $\uparrow$ TOA	[ $W\ m^{-2}$ ]	231	227	4	14	16	3	0.97
Net Flux TOA	[ $W\ m^{-2}$ ]	-14	-25	11	30	30	5	0.99
C_SW $\uparrow$ TOA	[ $W\ m^{-2}$ ]	42	38	4	3	3	2	0.96
SW CRE	[ $W\ m^{-2}$ ]	-50	-67	17	6	7	7	0.94
C_LW $\uparrow$ TOA	[ $W\ m^{-2}$ ]	249	258	-9	14	15	2	0.99
LW CRE	[ $W\ m^{-2}$ ]	18	31	-13	4	4	3	0.69
Net CRE	[ $W\ m^{-2}$ ]	-32	-37	5	4	6	6	0.96

Table 4 shows that the strongest correlations between model simulations and observations are found in reflected shortwave (SW $\uparrow$ ), absorbed shortwave (SW( $\downarrow\uparrow$ )), outgoing longwave radiation (OLR, LW $\uparrow$ ), net flux, clear-sky OLR (C\_LW $\uparrow$ ), and clear-sky reflected SW (C\_SW $\uparrow$ ), but show the weakest correlations in cloud fraction (CF) and total water path (TWP). Regional results over the SML (Table 5) differ somewhat from global counterparts, with much lower correlations of TWP, but increased correlations of CF, shortwave cloud radiative effect (CRESW), and net cloud radiative effect (CRENET) relative to global correlations.

Table 6. Global (GBL) weighted means and standard deviations for the GISS GCM and CERES-MODIS Observations separated into DJF and JJA seasons.

Variable	Units	GISS	OBS	GISS	OBS	Corr GBL DJF	GISS	OBS	GISS	OBS	Corr GBL JJA
		GBL Avg DJF	GBL Avg DJF	GBL Std Dev DJF	GBL Std Dev DJF		GBL Avg JJA	GBL Avg JJA	GBL Std Dev JJA	GBL Std Dev JJA	
CF	[%]	63	61	16	19	0.11	59	62	16	18	0.47
TWP	[ $g\ m^{-2}$ ]	183	121	128	90	0.47	193	116	132	80	0.42
SW $\uparrow$ TOA	[ $W\ m^{-2}$ ]	104	105	84	86	0.97	97	95	62	69	0.94
SW( $\downarrow$ - $\uparrow$ ) TOA	[ $W\ m^{-2}$ ]	248	245	131	129	0.99	235	236	120	122	0.98
LW $\uparrow$ TOA	[ $W\ m^{-2}$ ]	237	237	35	36	0.95	243	243	40	45	0.97
Net Flux TOA	[ $W\ m^{-2}$ ]	10	8	106	102	0.98	-8	-8	93	89	0.97
C_SW $\uparrow$ TOA	[ $W\ m^{-2}$ ]	56	54	86	82	0.99	50	50	46	55	0.95
SW CRE	[ $W\ m^{-2}$ ]	-49	-52	34	42	0.87	-47	-45	30	32	0.84
C_LW $\uparrow$ TOA	[ $W\ m^{-2}$ ]	255	263	41	42	0.99	261	270	44	47	0.99
LW CRE	[ $W\ m^{-2}$ ]	18	26	11	15	0.83	18	26	11	14	0.75
Net CRE	[ $W\ m^{-2}$ ]	-31	-26	29	37	0.85	-28	-18	25	29	0.83

Table 7. Same as Table 6, except for the Southern Mid-Latitudes (SML).

Variable	Units	GISS	OBS	GISS	OBS	Corr SML DJF	GISS	OBS	GISS	OBS	Corr SML JJA
		SML Avg DJF	SML Avg DJF	SML Std Dev DJF	SML Std Dev DJF		SML Avg JJA	SML Avg JJA	SML Std Dev JJA	SML Std Dev JJA	
CF	[%]	59	78	8	9	0.72	58	78	13	7	0.65
TWP	[ $g\ m^{-2}$ ]	195	178	38	52	0.29	214	217	70	70	0.15
SW $\uparrow$ TOA	[ $W\ m^{-2}$ ]	134	154	20	27	0.90	51	55	14	15	0.86
SW( $\downarrow$ - $\uparrow$ ) TOA	[ $W\ m^{-2}$ ]	341	318	33	39	0.96	98	94	47	45	0.99
LW $\uparrow$ TOA	[ $W\ m^{-2}$ ]	237	236	12	15	0.94	225	220	15	18	0.98
Net Flux TOA	[ $W\ m^{-2}$ ]	104	82	22	25	0.96	-126	-127	34	30	0.99
C_SW $\uparrow$ TOA	[ $W\ m^{-2}$ ]	55	48	6	4	0.79	28	26	6	5	0.86
SW CRE	[ $W\ m^{-2}$ ]	-80	-106	15	24	0.83	-23	-29	9	10	0.78
C_LW $\uparrow$ TOA	[ $W\ m^{-2}$ ]	255	263	13	14	0.99	244	254	15	16	0.99
LW CRE	[ $W\ m^{-2}$ ]	17	27	3.32	4	0.50	19	33	5	6	0.86
Net CRE	[ $W\ m^{-2}$ ]	-62	-79	15.56	24	0.92	-4	4	7	10	0.89

Global seasonal correlations in Table 6 are fairly consistent between DJF and JJA for most variables; however, an increase in CF correlation is shown during JJA (+0.36), while small increases in TWP (+0.06) and longwave cloud radiative effect (+0.08,  $CRE_{LW}$ ) correlations are found during DJF. Correlations in  $SW\uparrow$ ,  $SW(\downarrow\uparrow)$ , OLR ( $LW\uparrow$ ), net flux,  $C\_SW\uparrow$ , and clear-sky OLR ( $C\_LW\uparrow$ ) remain the strongest during both DJF and JJA, while CF shows to have the weakest correlation during the DJF season (0.12) with a moderate improvement during JJA (0.48).

SML seasonal correlations, shown in Table 7, show increases in correlation during the winter for  $C\_SW\uparrow$  and  $CRE_{LW}$ , while only showing an increase in TWP correlation during the summer months. Many variables with the strongest correlations remained strong during both seasons:  $SW\uparrow$ ,  $SW(\downarrow\uparrow)$ , OLR ( $LW\uparrow$ ), net flux, clear-sky OLR ( $C\_LW\uparrow$ ), and  $CRE_{NET}$ ; however,  $CRE_{SW}$  showed a small decrease in correlation during both DJF and JJA, while  $C\_SW\uparrow$  correlation decreased during the winter (-0.21) compared to summer. TWP shows the weakest correlation in the winter (0.18), with a moderate improvement during the summer months (0.40).

Global and SML Taylor diagrams were produced based on the results shown in Table 4 and 5, to provide a quick visual tool for comparing GCM simulations and observations. In these Taylor diagrams, the observational reference point is along the horizontal axis with a set standard deviation value of 1. Each variable in the GCM is then placed within the Taylor diagram by its standard deviation, which is normalized by the observational standard deviation and given as the distance away from the origin (as in Jiang et al., 2012), and by the correlation between the GCM and observations, given by

the value along the arc. Distances between the GCM values and observations are then measured as the RMS of the difference between modeled and observed values.

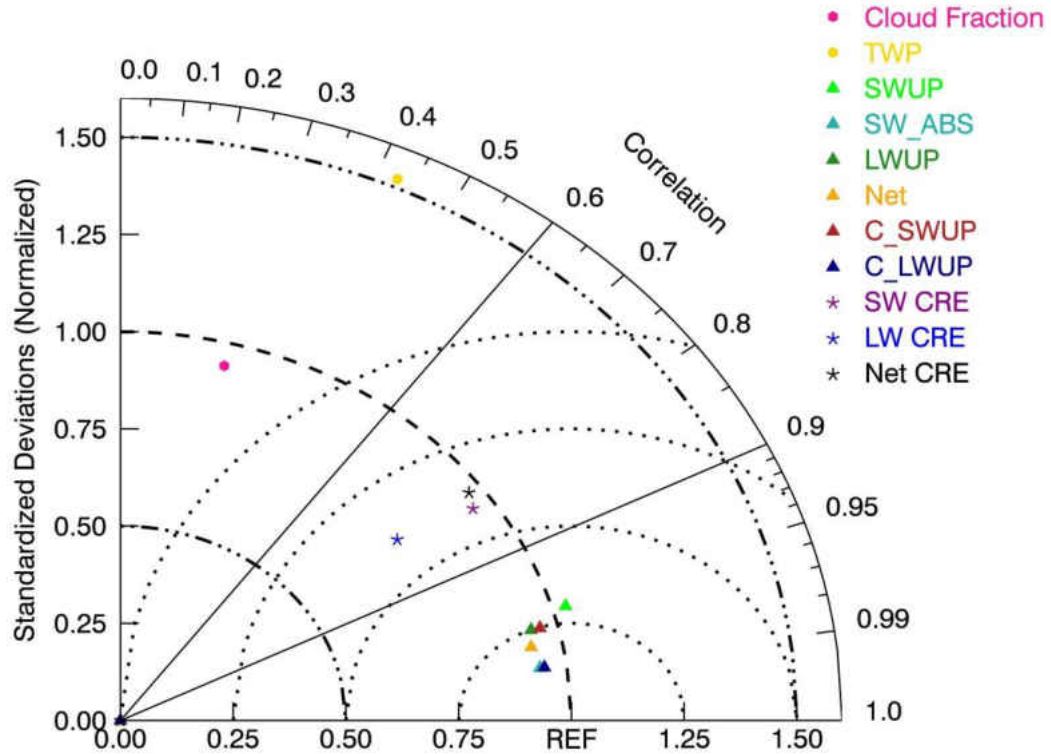


Figure 30. Taylor diagram showing the normalized global standard deviations and correlations between the GISS GCM and CERES-MODIS observations over the March 2000 to December 2005 time period.



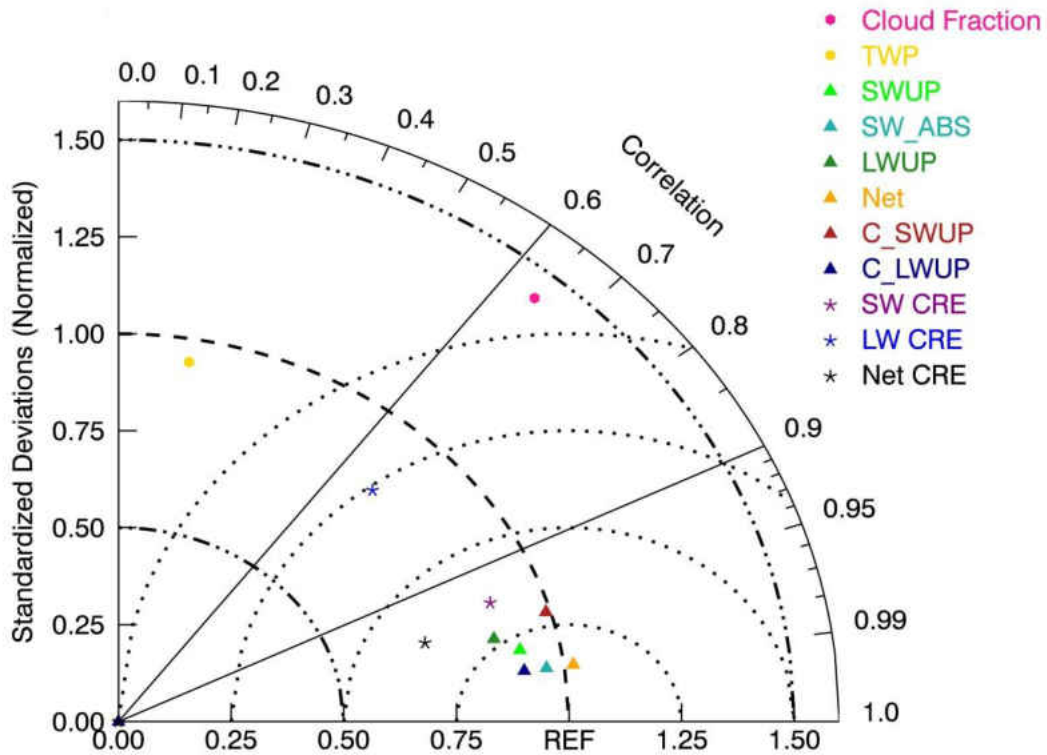


Figure 31. Same as Figure 30, except standard deviations and correlations are for the SML.

Based on the cloud property comparisons between the GCM and CERES-MODIS SYN1 observations globally and regionally, and also with comparisons to CloudSat/CALIPSO over the SML, the following conclusions were reached:

- 1) GISS-E2-R simulated cloud fraction, on global average, agrees with observations within 1%, however, large differences/biases are found over some regions. Over the SML focus region, cloud fraction is greatly undersimulated by the GCM by over 20%. Comparisons to SYN1-daily and CloudSat/CALIPSO vertical profiles showed the GCM in particular undersimulates low-level clouds over the SML. Undersimulated low-level clouds produce large impacts on the TOA radiation budget over the SML.

2) Total water path (TWP) is oversimulated  $70 \text{ g m}^{-2}$  globally by the GISS model compared to CERES SYN1 observations ( $188$  and  $118 \text{ g m}^{-2}$ , respectively). Over the SML however, the difference in TWP is small, with an oversimulation of only  $2 \text{ g m}^{-2}$  (GISS  $202$  and SYN1  $200 \text{ g m}^{-2}$ ). Since observed and modeled TWP values are equivalent, but simulated CF is lower, simulated clouds must be thicker than observed clouds.

Given this cloud property assessment, it is necessary to investigate how these differences impact the TOA radiation budgets. Therefore, the GISS modeled TOA radiation budgets are compared with CERES-MODIS EBAF results globally and regionally over the SML. These comparisons are conducted for the same time period of March 2000 through December 2005 with the following conclusions:

3) Since the fraction of highly reflective low-level clouds is undersimulated, the GISS model undersimulates reflected SW flux by  $-13 \text{ W m}^{-2}$  compared to observations ( $92$  and  $105 \text{ W m}^{-2}$ , respectively) over the SML. Reflected SW fluxes have a strong negative correlation with absorbed SW fluxes, showing an oversimulation of  $15 \text{ W m}^{-2}$  of SW radiation being absorbed over the SML. The impacts of low-level clouds on OLR are small (a difference of  $+3 \text{ W m}^{-2}$  model-observed) due to the minimal difference between sea surface temperatures and low-level cloud top temperatures. The negative SW bias and positive LW bias partially offset one another, resulting in a net bias of  $10 \text{ W m}^{-2}$ .

To quantitatively assess the impacts of clouds on the TOA radiation budget, clear-sky results were calculated first, and then combined with all-sky results to calculate cloud radiative effects (CREs) over the SML with the following conclusions:

- 4)  $CRE_{SW}$  cooling over the SML is drastically undersimulated ( $+17 \text{ W m}^{-2}$ ) by the GCM compared to observations ( $-50$  and  $-67 \text{ W m}^{-2}$  respectively). Simulated reflected shortwave for clear-sky conditions correlated fairly well with observations, suggesting that the large bias between the GCM and observations for shortwave CRE is caused by the undersimulation of all-sky reflected shortwave due to undersimulated low level clouds.
- 5)  $CRE_{LW}$  results show a negative bias of  $13 \text{ W m}^{-2}$  between the GCM and observations ( $18$  and  $31 \text{ W m}^{-2}$ , respectively). Given that only minor biases are present during all-sky OLR comparisons, the  $CRE_{LW}$  bias is mainly attributed to the clear-sky OLR bias. This bias is known to be due to a dry bias of  $10 \text{ W m}^{-2}$  in clear-sky OLR when comparing the GCM with observations over the SML. This is larger than the expected dry bias; however this is hypothesized to be due to the gross oversimulation of modeled atmospheric water vapor at the 100-mb level.
- 6) SW and LW CRE biases over the SML partially cancel out, leaving a bias of  $5 \text{ W m}^{-2}$  in  $CRE_{NET}$  between the model and observations ( $-32$  and  $-37 \text{ W m}^{-2}$ , respectively).

In conclusion, the GISS-E2-R GCM shows good agreement with observed cloud fraction and the TOA radiation budget on a global scale. However, this agreement is most likely due to the offsetting effect of different regional biases, given that large biases exist within the model. It is hoped that this study will highlight the problems within the GISS-E2-R GCM, which can be further analyzed to improve GCM simulations for global climate predictions and future IPCC assessment reports.

### *Future Work*

While this study shows the good agreement between model simulations and observations, large biases exist regionally, and further research must be done to explain why these biases exist.

To determine if the model biases exist due to dynamics, parameterizations, or a combination of two, a self-organizing map (SOM) will be developed over the SML following the method of Kennedy et al. (2012). This will show whether the model is indeed achieving the right atmospheric states to develop clouds over the SML, or the model is undersimulating clouds due to incorrect cloud microphysical parameterizations. To extend this research into model dynamics, further study will be done by running the model in Transpose AMIP (T-AMIP), which essentially runs the model in forecast mode as compared to the full-scale GCM. This will allow for detailed analysis of specific model physics and dynamics over the SML to examine cloud generation mechanisms, using model runs that can be completed much more quickly than running the full temporal-scale model.

NASA GISS has also agreed to provide much improved post-CMIP5 model results as well, allowing for a comparison of pre and post-CMIP5 versions of the model. It is expected that these comparisons will be submitted for publication within the next few months after this study.

## REFERENCES

- Bony, S., et al. (2006), How Well Do We Understand and Evaluate Climate Change Feedback Processes? *J. Climate*, 19(15), 3445-3482.
- Cess, R. D., et al (1989), Interpretation of Cloud-Climate Feedback as Produced by 14 Atmospheric General Circulation Models, *Science*, Volume 245, Issue 4917, pp. 513-516.
- Cess, R. D., et al. (1997), Comparison of the seasonal change in cloud-radiative forcing from atmospheric general circulation models and satellite observations, *J. Geophys. Res.*, 102, 16593-16603.
- Dong, X. and G. G. Mace (2003), Arctic Stratus Cloud Properties and Radiative Forcing Derived from Ground-Based Data Collected at Barrow, Alaska, *J. Climate*, 16(3), 445-461.
- Dong, X., B. Xi, and P. Minnis (2006), A Climatology of Midlatitude Continental Clouds from the ARM SGP Central Facility. Part II: Cloud Fraction and Surface Radiative Forcing, *J. Climate*, 19(9), 1765-1783.
- Dong, X., P. Minnis, B. Xi, S. Sun-Mack, and Y. Chen (2008), Comparison of CERES-MODIS stratus cloud properties with ground-based measurements at the DOE ARM Southern Great Plains site, *J. Geophys. Res.*, 113, D03204.
- Giannecchini, K., Dong, X., and Baike, X. (2013), Comparison of CERES-MODIS Edition-2 cloud properties with CloudSat/CALIPSO and ground-based measurements at the DOE ARM North Slope of Alaska site, *Manuscript in revision*.
- Hansen, J., M. Sato, R. Ruedy, K. Lo, D. W. Lea, and M. Medina-Elizade, (2006) Global temperature change, *Proceedings of the National Academy of Sciences*(- 39), 14288.
- Hartmann, D. L. (1994), *Global physical climatology*, Acad. Press, San Diego.
- Houghton, J. T., Y. Ding, D. J. Griggs, M. Noguer, P. J. van der Linden, X. Dai, K. Maskell, and C. A. Johnson, 2001: *Climate Change 2001: The Scientific Basis*. Cambridge University Press, 944 pp.
- Jiang, J. H., et al. (2012), Evaluation of cloud and water vapor simulations in CMIP5 climate models using NASA “A-Train” satellite observations, *J. Geophys. Res.*, 117, D14105.

- Jin, Y., W. B. Rossow, and D. P. Wylie (1996), Comparison of the climatologies of high-level clouds from HIRS and ISCCP, *J. Clim.*, 9, 2850–2879.
- Karlsson, J., G. Svensson, and H. Rodhe (2008), Cloud radiative forcing of subtropical low level clouds in global models, *Climate Dynamics*, 30(7), 779-788.
- Kennedy, A. (2011) Evaluation of a Single Column Model at the Southern Great Plains Climate Research Facility, *Dissertation*.
- Lin, J. (2007), The Double-ITCZ Problem in IPCC AR4 Coupled GCMs: Ocean-Atmosphere Feedback Analysis, *J. Climate*, 20(18), 4497-4525,.
- Loeb, N. G., B. A. Wielicki, D. R. Doelling, G. L. Smith, D. F. Keyes, S. Kato, N. Manalo-Smith, T. Wong, 2009, Toward Optimal Closure of the Earth's TOA Radiation Budget, *Journal of Climate*, 22, pg 748-766.
- Ramanathan, V., B. R. Barkstrom, and E. F. Harrison (1989), Climate and the Earth's Radiation Budget, *Phys Today*, 42(5), 22-32.
- Ramanathan, V., R. D. Cess, E. F. Harrison, P. Minnis, B. R. Barkstrom, E. Ahmad, and D. Hartmann (1989), Cloud-Radiative Forcing and Climate: Results from the Earth Radiation Budget Experiment, *Science*, 243(4887), 57-63.
- Randall, D.A., R.A. Wood, S. Bony, R. Colman, T. Fichefet, J. Fyfe, V. Kattsov, A. Pitman, J. Shukla, J. Srinivasan, R.J. Stouffer, A. Sumi and K.E. Taylor (2007): Climate Models and Their Evaluation. In: *Climate Change 2007: The Physical Science Basis. Contribution of Working Group I to the Fourth Assessment Report of the Intergovernmental Panel on Climate Change* [Solomon, S., D. Qin, M. Manning, Z. Chen, M. Marquis, K.B. Averyt, M.Tignor and H.L. Miller (eds.)]. Cambridge University Press, Cambridge, United Kingdom and New York, NY, USA.
- Rossow, W. B. and R. A. Schiffer (1999), Advances in Understanding Clouds from ISCCP, *Bull. Amer. Meteor. Soc.*, 80(11), 2261-2287,.
- Schmidt, G. A. et al. (2006), Present-Day Atmospheric Simulations Using GISS ModelE: Comparison to In Situ, Satellite, and Reanalysis Data, *J. Climate*, 19(2), 153-192.
- Sohn, B., J. Schmetz, R. Stuhlmann, and J. Lee (2006), Dry Bias in Satellite-Derived Clear-Sky Water Vapor and Its Contribution to Longwave Cloud Radiative Forcing, *J. Climate*, 19(21), 5570-5580.
- Sohn, B. and R. Bennartz (2008), Contribution of water vapor to observational estimates of longwave cloud radiative forcing, *J. Geophys. Res.*, 113, D20107.
- Stephens, G. L., et al. (2002), The CloudSat Mission and the A-Train, *Bull. Amer. Meteor. Soc.*, 83(12), 1771-1790.

Stephens, G. L. (2005), Cloud Feedbacks in the Climate System: A Critical Review, *J. Clim.*, 18(2), 237-273.

Stubenrauch, C. J., S. Cros, A. Guignard, and N. Lamquin (2010), A 6-year global cloud climatology from the Atmospheric InfraRed Sounder AIRS and a statistical analysis in synergy with CALIPSO and CloudSat, *Atmospheric Chemistry and Physics*, 10(15), 7197-7214.

Su, H. et al. (2012), Diagnosis of Regime-dependent Cloud Simulation Errors in CMIP5 Models Using “A-Train” Satellite Observations and Reanalysis Data, *Under review*.

Taylor, K. E., et al (2011) CMIP5 Data Reference Syntax (DRS) and Controlled Vocabularies, 1-14.

Wielicki, B. A., B. R. Barkstrom, E. F. Harrison, R. B. Lee, G. Louis Smith, and J. E. Cooper (1996), Clouds and the Earth's Radiant Energy System (CERES): An Earth Observing System Experiment, *Bull. Amer. Meteor. Soc.*, 77(5), 853-868.

Xi, B., X. Dong, P. Minnis, and M. M. Khaiyer (2010), A 10 year climatology of cloud fraction and vertical distribution derived from both surface and GOES observations over the DOE ARM SPG site, *J. Geophys. Res.*, 115, D12124.

Zhang, M. H., et al. (2005), Comparing clouds and their seasonal variations in 10 atmospheric general circulation models with satellite measurements, *J. Geophys. Res.*, 110, D15S02, doi:10.1029/2004JD005021.